Estimation of fracture weaknesses and integrated attenuation factors from azimuthal seismic data

Huaizhen Chen, Kristopher Innanen

ABSTRACT

Seismic wave propagation in fractured reservoirs exhibits anisotropy and attenuation that are related to fracture properties (e.g. fracture density) and fluid parameters (e.g., fluid moduli and viscosity). Based on the linear slip theory, we derive stiffness parameters for fractured and attenuative rocks, and present the integrated attenuation factors involving both host rock intrinsic attenuation and fracture-induced attenuation. Using the simplified stiffness parameters, we derive a linearized reflection coefficient in terms of fracture weaknesses and integrated attenuation factors. A two-step inversion approach is proposed, which involves an iterative damped least-squares algorithm to predict P- and S-wave moduli using angle gathers at the azimuthal angle approximately equal to fracture orientation azimuth, and a Bayesian inversion method to estimate fracture weaknesses and integrated attenuation factors from seismic amplitude differences among the data at different azimuthal angles. Tests on synthetic data confirm the proposed approach makes a stable inversion for fracture weaknesses and integrated attenuation factors in the presence of moderate data noise. The proposed approach is further confirmed on a fractured carbonate real data set, within which we observe that reasonable parameters (P- and S-wave moduli, fracture weaknesses and integrated attenuation factors) are determined. We conclude that the proposed inversion approach can provide reliable parameters for prediction of natural fractures and discrimination of fluid type.

INTRODUCTION

Natural fractures play an important role in migration and storage of hydrocarbons in reservoirs. The linear slip theory describes the effect of fractures on elastic parameters using fracture weaknesses or compliances (Schoenberg and Douma, 1988; Schoenberg and Sayers, 1995; Gurevich, 2003). The rock with a set of vertical and rotationally invariant fractures is equivalent to a horizontal transversely isotropic (HTI) medium, and its stiffness matrix is expressed in terms of the normal and tangential fracture weaknesses Δ_{N} and Δ_{T}. Combining the penny-shaped crack model Hudson (1980) and linear slip theory, Bakulin et al. (2000) related the normal and tangential fracture weaknesses to fracture properties (fracture density, fracture aspect ratio and fillings). Chen et al. (2017b) studied how the normal and tangential fracture weaknesses change in the case of water and oil saturated rocks, which shows that the normal fracture weakness difference between water and oil fractured rocks is relatively small. It indicates that the normal fracture weakness in not a sensitive indicator to discriminate water and oil saturated fractures. Hence, in the present study, we will involve the attenuation factor as an additional factor for fluid identification.

The inverse quality factor $1/Q$ related to seismic attenuation in rocks can be used to determine the type of fluid in reservoirs (Wu and Aki, 1989; Klimentos and McCann, 1990; Dvorkin et al., 1995; Gautam, 2003; Mavko et al., 2009; Rubino and Holliger, 2013; Vinci et al., 2014; Chen and Innanen, 2017). Intrinsic attenuation in the host rock and induced

attenuation exist while seismic wave propagates in porous rocks with fractures and cracks. Much work has been done to study how the attenuation affects the rock property and seismic wave propagation characteristic. Hudson et al. (1996) studied the effect of connection between cracks and pores on the overall property of a cracked rock, and they proposed two frequency-dependent response quantities related to fluid parameters (fluid bulk modulus and viscosity). Pointer et al. (2000) discussed how the distribution and saturation of cracks affect the response quantity, and modeled the influence of fluid parameters on seismic wave attenuation. In the case of equant porosity, Chapman (2003) developed a theory to incorporate meso-scale fractures into the analysis of frequency-dependent anisotropy. Brajanovski et al. (2006) analyzed P-wave attenuation in fluid saturated rocks with different values of normal fracture weakness, and studied the relationship between the inverse quality factor and frequency in case of low, intermediate and high frequencies, respectively. Based on the linear slip theory, Chichinina et al. (2006) proposed the complex normal and tangential fracture weaknesses that related to Q anisotropy. Using the complex fracture weaknesses, Chichinina et al. (2009) implemented the estimation of velocity and attenuation anisotropy from physical modeling data. However, the effect of intrinsic attenuation on the stiffness matrix of fracture porous rock and seismic wave propagation modeling and interpretation is being ignored.

In HTI media, azimuthal amplitude variation with offset (AVO) data are used to estimate Thomsen (1986) anisotropic parameters. Rüger (1997, 1998) derived an approximate expression of PP- wave reflection coefficient as a function of anisotropic parameters for HTI media. Shaw and Sen (2004, 2006) demonstrated a method to utilize a scattering function and perturbation in stiffness matrix to derive linearized reflection coefficients for weak anisotropic media. Using PP-wave approximate reflection coefficient, fracture prediction from observed seismic data has been implemented based on the azimuthal AVO (Bachrach et al., 2009; Downton and Roure, 2010; Chen et al., 2014a; Downton and Roure, 2015). In order to improve the accuracy of fracture weakness inversion, there are some studies focusing on utilization of different types of input data (e.g, azimuthal elastic impedances, Chen et al. 2014b, 2017a) or new parameterization of fracture weaknesses (e.g., relative changes in fracture weaknesses, Pan et al. 2017). Chen et al. (2017b) proposed to use amplitude differences among azimuthal data to implement seismic inversion, which can lead to a stable of estimation of the normal and tangential fracture weaknesses.

In this study, we first derive stiffness parameters that involve the intrinsic attenuation of the host rock and the fracture-induced attenuation based on the linear slip theory; then under the assumptions of small fracture weaknesses (Chen et al., 2017a) and low-loss media (i.e., $1/Q \ll 1$, Moradi and Innanen 2015), we simplify the derived stiffness parameters, and express perturbations in the simplified stiffness parameters in the case of an interface separating two anisotropic and attenuative media. Using the perturbations and a scattering function, we derive a linearized PP- wave reflection coefficient as a function of integrated attenuation factors and fracture weaknesses. Finally we propose a two-step inversion method to estimate elastic parameters (P- and S-wave moduli), integrated attenuation factors and fracture weaknesses from azimuthal seismic data. Synthetic tests indicate that the integrated attenuation factors and fracture weaknesses can be estimated stably in the case of seismic traces containing moderate noise/error, and a test on real data acquired over a fractured carbonate reservoir demonstrates that the proposed approach can estimate

reasonable parameters for fracture prediction and fluid discrimination.

THEORY AND METHOD

Stiffness parameters related to fracture weaknesses and attenuation

The elastic stiffness matrix of a homogeneous isotropic and elastic medium containing a set of parallel fractures with normals parallel to the x_1-axis is given by (Schoenberg and Douma, 1988; Schoenberg and Sayers, 1995)

$$\mathbf{C} = \begin{bmatrix} M(1-\Delta_{\mathrm{N}}) & \lambda(1-\Delta_{\mathrm{N}}) & \lambda(1-\Delta_{\mathrm{N}}) & 0 & 0 & 0 \\ \lambda(1-\Delta_{\mathrm{N}}) & M(1-\chi^2\Delta_{\mathrm{N}}) & \lambda(1-\chi\Delta_{\mathrm{N}}) & 0 & 0 & 0 \\ \lambda(1-\Delta_{\mathrm{N}}) & \lambda(1-\chi\Delta_{\mathrm{N}}) & M(1-\chi^2\Delta_{\mathrm{N}}) & 0 & 0 & 0 \\ 0 & 0 & 0 & \mu & 0 & 0 \\ 0 & 0 & 0 & 0 & \mu(1-\Delta_{\mathrm{T}}) & 0 \\ 0 & 0 & 0 & 0 & 0 & \mu(1-\Delta_{\mathrm{T}}) \end{bmatrix}, \tag{1}$$

where $M = \lambda + 2\mu$, $\chi = \lambda/M = 1 - 2g$, $g = \mu/M$, λ and μ are Lamé constants of the homogeneous isotropic and elastic host rock, and Δ_{N} and Δ_{T} are the normal and tangential fracture weaknesses.

Involving the intrinsic attenuation of the host rock and the fracture-induced attenuation, we present the complex stiffness matrix in terms of the complex normal and tangential fracture weaknesses and the complex moduli of the isotropic and attenuative background

$$\widetilde{\mathbf{C}} = \begin{bmatrix} \widetilde{M}(1-\widetilde{\Delta_{\mathrm{N}}}) & \widetilde{\lambda}(1-\widetilde{\Delta_{\mathrm{N}}}) & \widetilde{\lambda}(1-\widetilde{\Delta_{\mathrm{N}}}) & 0 & 0 & 0 \\ \widetilde{\lambda}(1-\widetilde{\Delta_{\mathrm{N}}}) & \widetilde{M}(1-\widetilde{\chi}^2\widetilde{\Delta_{\mathrm{N}}}) & \widetilde{\lambda}(1-\widetilde{\chi}\widetilde{\Delta_{\mathrm{N}}}) & 0 & 0 & 0 \\ \widetilde{\lambda}(1-\widetilde{\Delta_{\mathrm{N}}}) & \widetilde{\lambda}(1-\widetilde{\chi}\widetilde{\Delta_{\mathrm{N}}}) & \widetilde{M}(1-\widetilde{\chi}^2\widetilde{\Delta_{\mathrm{N}}}) & 0 & 0 & 0 \\ 0 & 0 & 0 & \widetilde{\mu} & 0 & 0 \\ 0 & 0 & 0 & 0 & \widetilde{\mu}(1-\widetilde{\Delta_{\mathrm{T}}}) & 0 \\ 0 & 0 & 0 & 0 & 0 & \widetilde{\mu}(1-\widetilde{\Delta_{\mathrm{T}}}) \end{bmatrix}, \tag{2}$$

where $\widetilde{M}$ and $\widetilde{\mu}$ are the complex compressional and shear moduli of the isotropic and attenuative background, $\widetilde{\lambda} = \widetilde{M} - 2\widetilde{\mu}$, and $\widetilde{\chi} = \widetilde{\lambda}/\widetilde{M}$. The complex normal and tangential fracture weaknesses, $\widetilde{\Delta_{\mathrm{N}}}$ and $\widetilde{\Delta_{\mathrm{T}}}$, are given by (Chichinina et al., 2006, 2009)

$$\begin{aligned} \widetilde{\Delta_{\mathrm{N}}} &= \Delta_{\mathrm{N}} - i\Delta_{\mathrm{N}}^{\mathrm{Im}} \\ \widetilde{\Delta_{\mathrm{T}}} &= \Delta_{\mathrm{T}} - i\Delta_{\mathrm{T}}^{\mathrm{Im}} \end{aligned}, \tag{3}$$

where Δ_{N} and Δ_{T}, and $\Delta_{\mathrm{N}}^{\mathrm{Im}}$ and $\Delta_{\mathrm{T}}^{\mathrm{Im}}$ represent the real and imaginary parts of fracture weaknesses, respectively, and the imaginary parts of fracture weaknesses are rewritten in terms of inverse quality factors

$$\begin{aligned} \Delta_{\mathrm{N}}^{\mathrm{Im}} &= \frac{1}{Q_{\mathrm{N}}}(1-\Delta_{\mathrm{N}}) \\ \Delta_{\mathrm{T}}^{\mathrm{Im}} &= \frac{1}{Q_{\mathrm{T}}}(1-\Delta_{\mathrm{T}}) \end{aligned}, \tag{4}$$

where $1/Q_{\mathrm{N}}$ and $1/Q_{\mathrm{T}}$ are fracture-induced inverse quality factors related to P- and S-wave attenuation in the direction perpendicular to fracture planes.

Substituting equation 4 into equation 2, we obtain the complex fracture weaknesses in terms of fracture-induced inverse quality factors

$$\begin{aligned}\widetilde{\Delta_{\mathrm{N}}} =&\Delta_{\mathrm{N}} - i\frac{1}{Q_{\mathrm{N}}}\Delta_{\mathrm{N}}\\ \widetilde{\Delta_{\mathrm{T}}} =&\Delta_{\mathrm{T}} - i\frac{1}{Q_{\mathrm{T}}}\Delta_{\mathrm{T}}\end{aligned}. \tag{5}$$

Hudson et al. (1996) presented a viscous cracked model to study the influence of cracks on the overall property of a cracked and porous rock. Pointer et al. (2000) proposed explicit expressions of two complex crack parameters related to crack properties (crack density and aspect ratio) and fluid parameters (fluid viscosity and moduli). Chichinina et al. (2006) expressed the complex normal and tangential fracture weaknesses as

$$\begin{aligned}\widetilde{\Delta_{\mathrm{N}}} &= \frac{4e}{3g(1-g)}\frac{1}{1+\widetilde{\Psi}(\omega)}\\ \widetilde{\Delta_{\mathrm{T}}} &= \frac{16e}{3(3-2g)}\frac{1}{1+\widetilde{\Omega}(\omega)}\end{aligned}, \tag{6}$$

where e is fracture density, and $\widetilde{\Psi}(\omega)$ and $\widetilde{\Omega}(\omega)$ are frequency-dependent quantities related to fluid parameters (See Appendix A). Pointer et al. (2000). demonstrated that at the low frequency (e.g. the seismic frequency range from 1-100Hz), $\widetilde{\Omega}(\omega)$ is approximately equal to zero. In this study, we set $\widetilde{\Delta_{\mathrm{T}}}$ to be real and $1/Q_{\mathrm{T}}$ to be zero in the case of seismic frequency range.

We next re-express the complex compressional and shear moduli $\widetilde{M}$ and $\widetilde{\mu}$. Under the assumption of low-loss viscoelastic host rock (i.e., P- and S-wave inverse quality factors $1/Q_{\mathrm{P}}$ and $1/Q_{\mathrm{S}}$ are much smaller than unity), Moradi and Innanen (2015) proposed the complex P- and S-wave velocities $\widetilde{\alpha}$ and $\widetilde{\beta}$

$$\begin{aligned}\widetilde{\alpha} &= \alpha_{\mathrm{E}}\left(1+i\frac{1}{2Q_{\mathrm{P}}}\right)\\ \widetilde{\beta} &= \beta_{\mathrm{E}}\left(1+i\frac{1}{2Q_{\mathrm{S}}}\right)\end{aligned}, \tag{7}$$

where α_{E} and β_{E} are P- and S-wave velocities. The inverse quality factors $1/Q_{\mathrm{P}}$ and $1/Q_{\mathrm{S}}$ are related to P- and S-wave attenuation while propagating in the isotropic and attenuative background.

Using the complex P- and S-wave velocities, we express the compressional and shear wave moduli neglecting high order terms of $1/Q_{\mathrm{P}}$ and $1/Q_{\mathrm{S}}$ under the assumption of low

loss medium

$$\begin{aligned}\widetilde{M} &= \rho(\widetilde{\alpha})^2 \approx M\left(1+i\frac{1}{Q_{\mathrm{P}}}\right)\\ \widetilde{\mu} &= \rho(\widetilde{\beta})^2 \approx \mu\left(1+i\frac{1}{Q_{\mathrm{S}}}\right)\end{aligned}. \tag{8}$$

Substituting equations 5 and 8 into equation 2 yields a new expression of the complex stiffness matrix

$$\widetilde{\mathbf{C}} = \begin{bmatrix} \widetilde{C_{11}} & \widetilde{C_{12}} & \widetilde{C_{12}} & 0 & 0 & 0\\ \widetilde{C_{12}} & \widetilde{C_{33}} & \widetilde{C_{23}} & 0 & 0 & 0\\ \widetilde{C_{12}} & \widetilde{C_{23}} & \widetilde{C_{33}} & 0 & 0 & 0\\ 0 & 0 & 0 & \widetilde{C_{44}} & 0 & 0\\ 0 & 0 & 0 & 0 & \widetilde{C_{55}} & 0\\ 0 & 0 & 0 & 0 & 0 & \widetilde{C_{66}} \end{bmatrix}, \tag{9}$$

where

$$\widetilde{C_{11}} = \left(M-\frac{M}{Q_{\mathrm{PN}}}\right)(1-\Delta_{\mathrm{N}}) + i\left(\frac{M}{Q_{\mathrm{P}}}+\frac{M}{Q_{\mathrm{N}}}\right)(1-\Delta_{\mathrm{N}}),$$

$$\widetilde{C_{12}} = \left(\lambda-\frac{M}{Q_{\mathrm{PN}}}+\frac{2\mu}{Q_{\mathrm{SN}}}\right)(1-\Delta_{\mathrm{N}}) + i\left(\frac{M}{Q_{\mathrm{P}}}-\frac{2\mu}{Q_{\mathrm{S}}}+\frac{\lambda}{Q_{\mathrm{N}}}\right)(1-\Delta_{\mathrm{N}}),$$

$$\begin{aligned}\widetilde{C_{23}} =&\lambda(1-\Delta_{\mathrm{N}}) + 2\lambda g\Gamma_1\Delta_{\mathrm{N}} + 2\lambda g\Gamma_2\frac{1-\Delta_{\mathrm{N}}}{Q_{\mathrm{N}}} - M\frac{1-\Delta_{\mathrm{N}}}{Q_{\mathrm{PN}}} + 2Mg\Gamma_1\frac{1-\Delta_{\mathrm{N}}}{Q_{\mathrm{PN}}}\\ &- 2Mg\Gamma_2\frac{\Delta_{\mathrm{N}}}{Q_{\mathrm{P}}} + 2\mu\frac{1-\Delta_{\mathrm{N}}}{Q_{\mathrm{SN}}} - 4\mu g\Gamma_1\frac{1-\Delta_{\mathrm{N}}}{Q_{\mathrm{SN}}} + 4\mu g\Gamma_2\frac{\Delta_{\mathrm{N}}}{Q_{\mathrm{S}}}\\ &+ i\begin{bmatrix}\lambda\dfrac{1-\Delta_{\mathrm{N}}}{Q_{\mathrm{N}}} - 2\lambda g\Gamma_1\dfrac{1-\Delta_{\mathrm{N}}}{Q_{\mathrm{N}}} + 2\lambda g\Gamma_2\Delta_{\mathrm{N}} + M\dfrac{1-\Delta_{\mathrm{N}}}{Q_{\mathrm{P}}} + 2Mg\Gamma_1\dfrac{\Delta_{\mathrm{N}}}{Q_{\mathrm{P}}}\\ +2Mg\Gamma_2\dfrac{1-\Delta_{\mathrm{N}}}{Q_{\mathrm{PN}}} - 2\mu\dfrac{1-\Delta_{\mathrm{N}}}{Q_{\mathrm{S}}} + \Gamma_1\Delta_{\mathrm{N}} - 4\mu g\Gamma_2\dfrac{1-\Delta_{\mathrm{N}}}{Q_{\mathrm{SN}}}\end{bmatrix},\end{aligned}$$

$$\begin{aligned}\widetilde{C_{33}} =&M(1-\Delta_{\mathrm{N}}) + 4Mg\Gamma_1\Delta_{\mathrm{N}} + 4Mg\Gamma_2\frac{1-\Delta_{\mathrm{N}}}{Q_{\mathrm{N}}} - 4Mg^2\Gamma_1^2\Delta_{\mathrm{N}} - 8Mg^2\Gamma_1\Gamma_2\frac{1-\Delta_{\mathrm{N}}}{Q_{\mathrm{N}}}\\ &+ 4Mg^2\Gamma_2^2\Delta_{\mathrm{N}} - 4Mg\Gamma_2\frac{\Delta_{\mathrm{N}}}{Q_{\mathrm{P}}} + 4Mg\Gamma_1\frac{1-\Delta_{\mathrm{N}}}{Q_{\mathrm{PN}}} - 4Mg^2\Gamma_1^2\frac{1-\Delta_{\mathrm{N}}}{Q_{\mathrm{PN}}}\\ &+ 8Mg^2\Gamma_1\Gamma_2\frac{\Delta_{\mathrm{N}}}{Q_{\mathrm{P}}} + 4Mg^2\Gamma_2^2\frac{1-\Delta_{\mathrm{N}}}{Q_{\mathrm{PN}}}\\ &+ i\begin{bmatrix}M\dfrac{1-\Delta_{\mathrm{N}}}{Q_{\mathrm{N}}} + 4Mg\Gamma_2\Delta_{\mathrm{N}} - 4Mg\Gamma_1\dfrac{1-\Delta_{\mathrm{N}}}{Q_{\mathrm{N}}} + 4Mg^2\Gamma_1^2\dfrac{1-\Delta_{\mathrm{N}}}{Q_{\mathrm{N}}} - 8Mg^2\Gamma_1\Gamma_2\Delta_{\mathrm{N}}\\ -4Mg^2\Gamma_2^2\dfrac{1-\Delta_{\mathrm{N}}}{Q_{\mathrm{N}}} + M\dfrac{1-\Delta_{\mathrm{N}}}{Q_{\mathrm{P}}} + 4Mg\Gamma_1\dfrac{\Delta_{\mathrm{N}}}{Q_{\mathrm{P}}} + 4Mg\Gamma_2\dfrac{1-\Delta_{\mathrm{N}}}{Q_{\mathrm{PN}}} - 4Mg^2\Gamma_1^2\dfrac{\Delta_{\mathrm{N}}}{Q_{\mathrm{P}}}\\ -8Mg^2\Gamma_1\Gamma_2\dfrac{1-\Delta_{\mathrm{N}}}{Q_{\mathrm{PN}}} + 4Mg^2\Gamma_2^2\dfrac{\Delta_{\mathrm{N}}}{Q_{\mathrm{P}}} + M\dfrac{1-\Delta_{\mathrm{N}}}{Q_{\mathrm{PN}}}\end{bmatrix},\end{aligned}$$

$$\widetilde{C_{44}} = \mu + i\frac{\mu}{Q_{\mathrm{s}}},$$

$$\widetilde{C_{55}} = \mu(1-\Delta_{\mathrm{T}}) + i\frac{\mu}{Q_{\mathrm{s}}}(1-\Delta_{\mathrm{T}}), \tag{10}$$

and where $g = \mu/M$, $\Gamma_1 = \left(1+\frac{1}{Q_{\mathrm{P}}Q_{\mathrm{S}}}\right) / \left(1+\frac{1}{Q_{\mathrm{P}}^2}\right)$, $\Gamma_2 = \left(\frac{1}{Q_{\mathrm{S}}} - \frac{1}{Q_{\mathrm{P}}}\right) / \left(1+\frac{1}{Q_{\mathrm{P}}^2}\right)$. The quantities $\frac{1}{Q_{\mathrm{PN}}} = \frac{1}{Q_{\mathrm{P}}}\frac{1}{Q_{\mathrm{N}}}$ and $\frac{1}{Q_{\mathrm{SN}}} = \frac{1}{Q_{\mathrm{S}}}\frac{1}{Q_{\mathrm{N}}}$, which are P- and S-wave integrated attenuation factors, respectively.

We next study how the parameters Γ_1 and Γ_2 vary in the case of small P- and S-wave inverse quality factors in the background (i.e. $1/Q_{\mathrm{P}} \ll 1$ and $1/Q_{\mathrm{S}} \ll 1$). We employ an experimental formula given by Mavko et al. (2009) to compute $1/Q_{\mathrm{S}}$

$$\frac{1/Q_{\mathrm{P}}}{1/Q_{\mathrm{S}}} = \frac{\mu}{M}\left[\frac{4}{3} + \frac{5}{4}\frac{(M/\mu - 2/3)(M/\mu - 4/3)^2}{M/\mu - 8/9}\right]. \tag{11}$$

We plot variations of Γ_1 and Γ_2 with the P-wave inverse quality factor $1/Q_{\mathrm{P}}$ and the moduli ratio g, as shown in Figure 1.

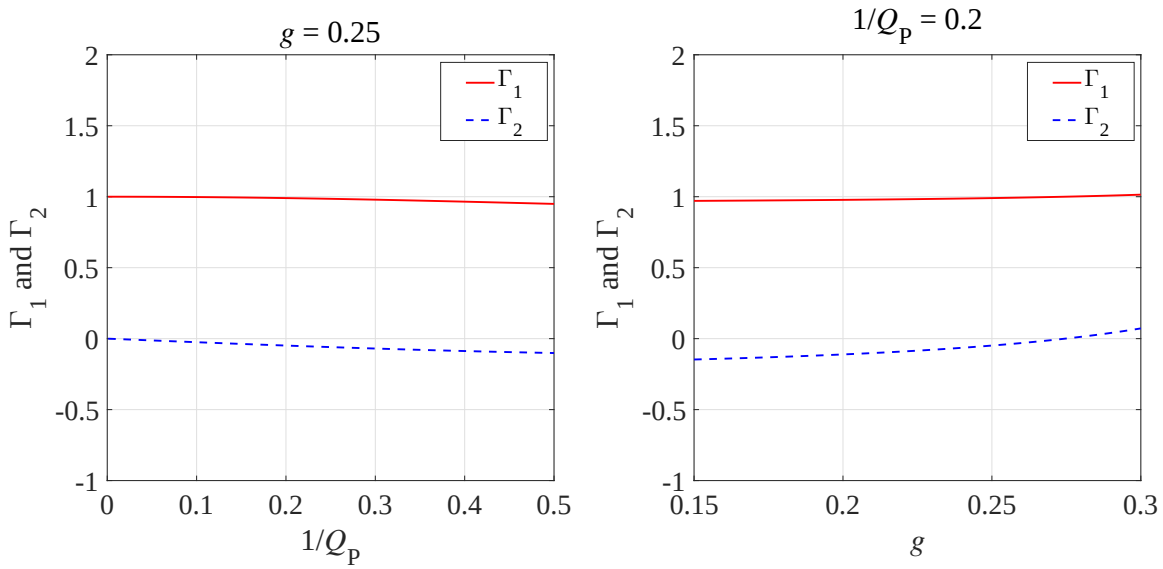

FIG. 1. Variations of Γ_1 and Γ_2 with P-wave inverse quality factors and the moduli ratio.

We observe that in the case of small inverse quality factors, Γ_1 is approximately equal to unity, and Γ_2 is approximately equal to zero. Also, under the assumption of small fracture weaknesses, we neglect the term proportional to $\Delta_{\mathrm{N}}/Q_{\mathrm{P}}$, $\Delta_{\mathrm{N}}/Q_{\mathrm{S}}$ and $\Delta_{\mathrm{T}}/Q_{\mathrm{S}}$. The simplified complex stiffness parameters are given by

$$\widetilde{C_{11}} \approx M - \frac{M}{Q_{\mathrm{PN}}} - M\Delta_{\mathrm{N}} + i\left(\frac{M}{Q_{\mathrm{P}}} + \frac{M}{Q_{\mathrm{N}}} - \frac{M}{Q_{\mathrm{N}}}\Delta_{\mathrm{N}}\right),$$

$$\widetilde{C_{12}} \approx \lambda - \lambda\Delta_{\mathrm{N}} - \frac{M}{Q_{\mathrm{PN}}} + \frac{2\mu}{Q_{\mathrm{SN}}} + i\left(\frac{M}{Q_{\mathrm{P}}} - \frac{2\mu}{Q_{\mathrm{S}}} + \frac{\lambda}{Q_{\mathrm{N}}} - \frac{\lambda}{Q_{\mathrm{N}}}\Delta_{\mathrm{N}}\right),$$

$$\begin{aligned}
\widetilde{C_{23}} \approx & \lambda(1-\Delta_{\mathrm{N}}) + 2\lambda g\Delta_{\mathrm{N}} - \frac{M}{Q_{\mathrm{PN}}} + 2Mg\frac{1}{Q_{\mathrm{PN}}} + 2\mu\frac{1}{Q_{\mathrm{SN}}} - 4\mu g\frac{1}{Q_{\mathrm{SN}}} \\
& + i\left[\lambda\frac{1-\Delta_{\mathrm{N}}}{Q_{\mathrm{N}}} - 2\lambda g\frac{1-\Delta_{\mathrm{N}}}{Q_{\mathrm{N}}} + 2\lambda g\Gamma_2\Delta_{\mathrm{N}} + M\frac{1}{Q_{\mathrm{P}}} - 2\mu\frac{1}{Q_{\mathrm{S}}} + \Delta_{\mathrm{N}}\right], \\
\widetilde{C_{33}} \approx & M(1-\Delta_{\mathrm{N}}) + 4Mg\Delta_{\mathrm{N}} - 4Mg^2\Delta_{\mathrm{N}} + 4Mg\frac{1}{Q_{\mathrm{PN}}} - 4Mg^2\frac{1}{Q_{\mathrm{PN}}} \\
& + i\left[M\frac{1-\Delta_{\mathrm{N}}}{Q_{\mathrm{N}}} - 4Mg\frac{1-\Delta_{\mathrm{N}}}{Q_{\mathrm{N}}} + 4Mg^2\frac{1-\Delta_{\mathrm{N}}}{Q_{\mathrm{N}}} + M\frac{1}{Q_{\mathrm{P}}} + M\frac{1}{Q_{\mathrm{PN}}}\right], \\
\widetilde{C_{44}} = & \mu + i\frac{\mu}{Q_{\mathrm{s}}}, \\
\widetilde{C_{55}} \approx & \mu - \mu\Delta_{\mathrm{T}} + i\frac{\mu}{Q_{\mathrm{s}}}.
\end{aligned} \tag{12}$$

Derivation of real P-to-P linearized reflection coefficient

Using the derived and simplified complex stiffness parameters (equation 12), we first express perturbations in stiffness parameters for the case of a reflection interface separating two fractured and attenuative layers. Chen and Innanen (2017) demonstrated that the imaginary part of the reflection coefficient is much smaller than the real part. Hence, in the present study, we focus on the derivation of the real part of P-to-P reflection coefficient. The real parts of perturbations in the complex stiffness parameters are given by

$$\begin{aligned}
\Delta\widetilde{C_{11}} = & \Delta M - \frac{\Delta M}{Q_{\mathrm{PN}}} - M\Delta\frac{1}{Q_{\mathrm{PN}}} - \Delta M\Delta_{\mathrm{N}} - M\delta_{\Delta_{\mathrm{N}}}, \\
\Delta\widetilde{C_{12}} = & \Delta\lambda - \Delta\lambda\Delta_{\mathrm{N}} - \lambda\delta_{\Delta_{\mathrm{N}}} - \frac{\Delta M}{Q_{\mathrm{PN}}} - M\Delta\frac{1}{Q_{\mathrm{PN}}} + \frac{2\Delta\mu}{Q_{\mathrm{SN}}} + 2\mu\Delta\frac{1}{Q_{\mathrm{SN}}}, \\
\Delta\widetilde{C_{23}} = & \Delta\lambda - \Delta\lambda\Delta_{\mathrm{N}} - \lambda\delta_{\Delta_{\mathrm{N}}} + 2g\Delta\lambda\Delta_{\mathrm{N}} + 2\lambda g\delta_{\Delta_{\mathrm{N}}} + (2g-1)\Delta M\frac{1}{Q_{\mathrm{PN}}} \\
& + (2g-1)M\Delta\frac{1}{Q_{\mathrm{PN}}} + (2-4g)\Delta\mu\frac{1}{Q_{\mathrm{SN}}} + (2-4g)\mu\Delta\frac{1}{Q_{\mathrm{SN}}}, \\
\Delta\widetilde{C_{33}} = & \Delta M - \Delta M\Delta_{\mathrm{N}} - M\delta_{\Delta_{\mathrm{N}}} + (4g-4g^2)\Delta M\Delta_{\mathrm{N}} + (4g-4g^2)M\delta_{\Delta_{\mathrm{N}}} \\
& + (4g-4g^2)\Delta M\frac{1}{Q_{\mathrm{PN}}} + (4g-4g^2)M\Delta\frac{1}{Q_{\mathrm{PN}}}, \\
\Delta\widetilde{C_{44}} = & \Delta\mu, \\
\Delta\widetilde{C_{55}} = & \Delta\mu - \Delta\mu\Delta_{\mathrm{T}} - \mu\delta_{\Delta_{\mathrm{T}}},
\end{aligned} \tag{13}$$

where ΔM is perturbation in the compressional modulus across the interface, $\Delta\lambda$ and $\Delta\mu$ are changes in Lamé constants across the interface, $\delta_{\Delta_{\mathrm{N}}}$ and $\delta_{\Delta_{\mathrm{T}}}$ are changes in the normal and tangential fracture weaknesses across the interface, and $\Delta(1/Q_{\mathrm{PN}})$ and $\Delta(1/Q_{\mathrm{SN}})$ are changes in the integrated attenuation factors.

Under the assumptions of small fracture weaknesses and small changes in LamÃl' constants across the interface, we neglect the term proportional to $\Delta\lambda\Delta_{\rm N}$, $\Delta\mu\Delta_{\rm N}$ and $\Delta\mu\Delta_{\rm T}$ to simplify the perturbations in stiffness parameters

$$\begin{aligned}
\Delta\widetilde{C_{11}} &\approx \Delta M - \frac{\Delta M}{Q_{\rm PN}} - M\Delta\frac{1}{Q_{\rm PN}} - M\delta_{\Delta_{\rm N}},\\
\Delta\widetilde{C_{12}} &\approx \Delta\lambda - \lambda\delta_{\Delta_{\rm N}} - \frac{\Delta M}{Q_{\rm PN}} - M\Delta\frac{1}{Q_{\rm PN}} + \frac{2\Delta\mu}{Q_{\rm SN}} + 2\mu\Delta\frac{1}{Q_{\rm SN}},\\
\Delta\widetilde{C_{23}} \approx& \Delta\lambda - \lambda\delta_{\Delta_{\rm N}} + (2g-1)\Delta M\frac{1}{Q_{\rm PN}} + (2g-1)M\Delta\frac{1}{Q_{\rm PN}}\\
&+ (2-4g)\Delta\mu\frac{1}{Q_{\rm SN}} + (2-4g)\mu\Delta\frac{1}{Q_{\rm SN}},\\
\Delta\widetilde{C_{33}} \approx& \Delta M - M\delta_{\Delta_{\rm N}} + (4g-4g^2)M\delta_{\Delta_{\rm N}}\\
&+ (4g-4g^2)\Delta M\frac{1}{Q_{\rm PN}} + (4g-4g^2)M\Delta\frac{1}{Q_{\rm PN}},\\
\Delta\widetilde{C_{44}} &= \Delta\mu,\\
\Delta\widetilde{C_{55}} &\approx \Delta\mu - \mu\delta_{\Delta_{\rm T}}.
\end{aligned} \tag{14}$$

Shaw and Sen (2004, 2006) proposed a method to use the scattering function involving perturbation in stiffness matrix to derive linearized reflection coefficients. The relationship between the P-to-P reflection coefficient and the scattering function is given by

$$R_{PP} = \frac{1}{4\rho\cos^2\theta}S, \tag{15}$$

where θ is P-wave incidence angle, ρ is the density of the elastic isotropic background, and S is the scattering function that is given by

$$\begin{aligned}
S =& \Delta\rho\cos2\theta + \Delta C_{11}\xi_{11} + \Delta C_{12}(\xi_{12}+\xi_{13}+\xi_{21}+\xi_{31})\\
&+ \Delta C_{23}(\xi_{23}+\xi_{32}) + \Delta C_{33}(\xi_{22}+\xi_{33}) + \Delta C_{44}\xi_{44} + \Delta C_{55}(\xi_{55}+\xi_{66}),
\end{aligned} \tag{16}$$

where $\Delta\rho$ is the perturbation in density across the interface, and the elements of ξ are given by Shaw and Sen (2006)

$$\begin{aligned}
\xi_{11} &= \frac{\rho\sin^4\theta\cos^4\phi}{M}, \xi_{12} = \frac{\rho\sin^4\theta\sin^2\phi\cos^2\phi}{M}, \xi_{13} = \frac{\rho\sin^2\theta\cos^2\theta\cos^2\phi}{M},\\
\xi_{21} &= \xi_{12}, \xi_{22} = \frac{\rho\sin^4\theta\sin^4\phi}{M}, \xi_{23} = \frac{\rho\sin^2\theta\cos^2\theta\sin^2\phi}{M},\\
\xi_{31} &= \xi_{13}, \xi_{32} = \xi_{23}, \xi_{33} = \frac{\rho\cos^4\theta}{M},\\
\xi_{44} &= \frac{-4\rho\sin^2\theta\cos^2\theta\sin^2\phi}{M}, \xi_{55} = \frac{-4\rho\sin^2\theta\cos^2\theta\cos^2\phi}{M}, \xi_{66} = \frac{4\sin^4\theta\sin^2\phi\cos^2\phi}{\alpha^2},
\end{aligned} \tag{17}$$

where ϕ is the azimuthal angle between the fracture symmetry axis and the source-receiver line. It is important to stress that both the incidence and azimuthal angels are the phase angles. Combining equations 13-17, we obtain the linearized P-to-P complex reflection coefficient

$$R_{\rm PP}(\theta,\phi) = R_{\rm PP}^{\rm iso-elastic}(\theta) + R_{\rm PP}^{\rm ani-visco}(\theta,\phi), \tag{18}$$

where $R_{\rm PP}^{\rm iso-elastic}(\theta)$ is the reflection coefficient only related to the elastic properties of the isotropic and elastic background, and $R_{\rm PP}^{\rm ani-visco}(\theta,\phi)$ is the reflection coefficient involving the effects of attenuation and fractures, and where

$$R_{\rm PP}^{\rm iso-elastic}(\theta) = P_M(\theta)\frac{\Delta M}{M} + P_\mu(\theta)\frac{\Delta\mu}{\mu} + P_\rho(\theta)\frac{\Delta\rho}{\rho}, \tag{19}$$

$$\begin{aligned} R_{\rm PP}^{\rm ani-visco}(\theta,\phi) =& P_{Q_{\rm PN}}(\theta,\phi)\Delta\frac{1}{Q_{\rm PN}} + P_{Q_{\rm SN}}(\theta,\phi)\Delta\frac{1}{Q_{\rm SN}} \\ &+ P_{\Delta_{\rm N}}(\theta,\phi)\delta_{\Delta_{\rm N}} + P_{\Delta_{\rm T}}(\theta,\phi)\delta_{\Delta_{\rm T}}, \end{aligned} \tag{20}$$

in which

$$\begin{aligned} P_M(\theta) =& \frac{1}{4}\sec^2\theta, P_\mu(\theta) = -2g\sin^2\theta, P_\rho(\theta) = \frac{\cos 2\theta}{4\cos^2\theta}, \\ P_{Q_{\rm PN}}(\theta,\phi) =& \frac{1}{4}\sec^2\theta\begin{bmatrix} -\sin^4\theta\cos^2\phi(1+\sin^2\phi) + 2\sin^2\theta\cos^2\theta(2g\sin^2\phi - 1) \\ +4g(1-g)(\sin^4\theta\sin^4\phi + \cos^4\theta) \end{bmatrix}, \\ P_{Q_{\rm SN}}(\theta,\phi) =& g\sin^2\theta(\tan^2\theta\sin^2\phi\cos^2\phi + 1 - 2g\sin^2\phi) \\ P_{\Delta_{\rm N}}(\theta,\phi) =& -\frac{1}{4}\sec^2\theta[1 - 2g(\sin^2\theta\sin^2\phi + \cos^2\theta)]^2, \\ P_{\Delta_{\rm T}}(\theta,\phi) =& g\sin^2\theta\cos^2\phi(1 - \tan^2\theta\sin^2\phi). \end{aligned} \tag{21}$$

The quantities $\frac{\Delta M}{M}$, $\frac{\Delta\mu}{\mu}$ and $\frac{\Delta\rho}{\rho}$ are reflectivities of P- and S-wave moduli and density, $\Delta(1/Q_{\rm PN})$ and $\Delta(1/Q_{\rm SN})$ are changes in the integrated attenuation factors across the interface, $\delta_{\Delta_{\rm N}}$ and $\delta_{\Delta_{\rm T}}$ are changes in the normal and tangential fracture weaknesses across the interface.

Estimation of integrated attenuation factors from seismic data

We proceed to the method to estimate the integrated attenuation factors and fracture weaknesses from observed seismic data. In the present study, we propose a two-step inversion approach to use azimuthal seismic amplitudes to predict elastic parameters (P- and S-wave moduli M and μ), integrated attenuation factors ($1/Q_{\rm PN}$ and $1/Q_{\rm SN}$) and fracture weaknesses ($\Delta_{\rm N}$ and $\Delta_{\rm T}$). Figure 2 plots the workflow of the two-step inversion approach.

We first use seismic data along fracture orientation azimuth to estimate the elastic parameters. Using the reflection coefficient $R_{\rm PP}^{\rm iso-elastic}(\theta)$ in equation 19, we express the generation of seismic data in matrix for the case of k incidence angle and n reflection interface

$$\mathbf{d} = \mathbf{G}\mathbf{m}, \tag{22}$$

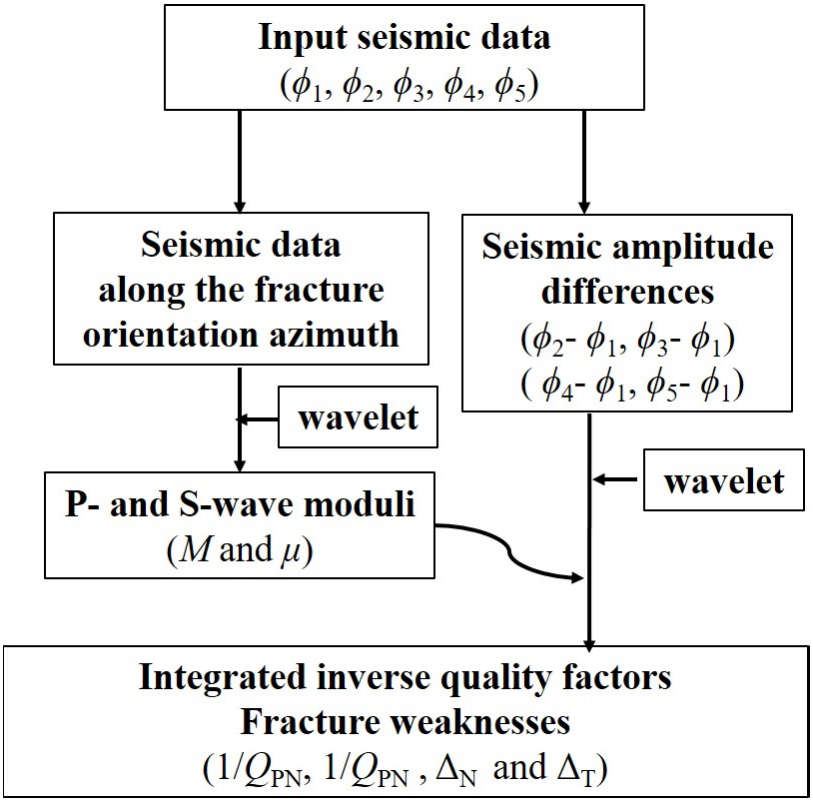

FIG. 2. Workflow of two-step inversion approach

where

$$\mathbf{d} = \begin{bmatrix} \mathbf{s}(\theta_1) \\ \vdots \\ \mathbf{s}(\theta_k) \end{bmatrix}_{kn\times 1}, \ \mathbf{G} = \begin{bmatrix} \mathbf{WP}_M(\theta_1) & \mathbf{WP}_\mu(\theta_1) & \mathbf{WP}_\rho(\theta_1) \\ \vdots & \vdots & \vdots \\ \mathbf{WP}_M(\theta_k) & \mathbf{WP}_\mu(\theta_k) & \mathbf{WP}_\rho(\theta_k) \end{bmatrix}_{kn\times 3n}, \ \mathbf{m} = \begin{bmatrix} \mathbf{R}_M \\ \mathbf{R}_\mu \\ \mathbf{R}_\rho \end{bmatrix}_{\mathbf{3n\times 1}},$$

$$\mathbf{R}_M = \begin{bmatrix} \dfrac{\Delta M_1}{M_1} \\ \vdots \\ \dfrac{\Delta M_n}{M_n} \end{bmatrix}_{n\times 1}, \ \mathbf{R}_\mu = \begin{bmatrix} \dfrac{\Delta \mu_1}{\mu_1} \\ \vdots \\ \dfrac{\Delta \mu_n}{\mu_n} \end{bmatrix}_{n\times 1}, \ \mathbf{R}_\rho = \begin{bmatrix} \dfrac{\Delta \rho_1}{\rho_1} \\ \vdots \\ \dfrac{\Delta \rho_n}{\rho_n} \end{bmatrix}_{n\times 1}, \ \mathbf{W} = \begin{bmatrix} w_1 & 0 & 0 & \dots \\ w_2 & w_1 & 0 & \ddots \\ w_3 & w_2 & w_1 & \ddots \\ \vdots & \ddots & \ddots & \ddots \end{bmatrix}_{n\times n},$$

$$\mathbf{s} = \begin{bmatrix} s_1 \\ \vdots \\ s_n \end{bmatrix}_{n\times 1}, \ \mathbf{P}_M = \begin{bmatrix} P_M(\theta) & & \\ & \ddots & \\ & & P_M(\theta) \end{bmatrix}_{n\times n}, \ \mathbf{P}_\mu = \begin{bmatrix} P_\mu(\theta, g_1) & & \\ & \ddots & \\ & & P_\mu(\theta, g_n) \end{bmatrix}_{n\times n},$$

$$\mathbf{P}_\rho = \begin{bmatrix} P_\rho(\theta) & & \\ & \ddots & \\ & & P_\rho(\theta) \end{bmatrix}_{n\times n}, \tag{23}$$

where s is a sample in the input seismic data set, and the quantity w_l is the l^{th} element of a vector containing the source wavelet.

The inverse problem is solved by the iterative damped least-squares algorithm

$$\mathbf{m} = \mathbf{m}_{\mathrm{mod}} + (\mathbf{G}^{\mathrm{T}}\mathbf{G} + \sigma^2)^{-1}\mathbf{G}^{\mathrm{T}}(\mathbf{d} - \mathbf{G}\mathbf{m}), \tag{24}$$

where $\mathbf{m}_{\mathrm{mod}}$ is the initial model, $\mathbf{G}^{\mathrm{T}}$ is the transpose of $\mathbf{G}$, and σ^2 is the damping factor related to the signal-to-noise ratio (SNR).

We next employ seismic amplitude differences among the input data at different azimuthal angles to estimate the integrated attenuation factors and fracture weaknesses. The seismic amplitude differences in the case of five azimuthal angles (i.e. ϕ_1, ϕ_2, ϕ_3, ϕ_4 and ϕ_5), k incidence angle and n reflection interface are given by

$$\mathbf{B} = \mathbf{A}\mathbf{X}, \tag{25}$$

where

$$\mathbf{B} = \begin{bmatrix} \mathbf{b}(\phi_2) - \mathbf{b}(\phi_1) \\ \mathbf{b}(\phi_3) - \mathbf{b}(\phi_1) \\ \mathbf{b}(\phi_4) - \mathbf{b}(\phi_1) \\ \mathbf{b}(\phi_5) - \mathbf{b}(\phi_1) \end{bmatrix}_{4kn\times 1}, \ \mathbf{X} = \begin{bmatrix} \mathbf{R}_{Q_{\mathrm{PN}}} \\ \mathbf{R}_{Q_{\mathrm{SN}}} \\ \mathbf{R}_{\Delta_{\mathrm{N}}} \\ \mathbf{R}_{\Delta_{\mathrm{T}}} \end{bmatrix}_{4n\times 1}, \ \mathbf{b}(\phi) = \begin{bmatrix} \mathbf{b}_1(\theta_1, \phi) \\ \vdots \\ \mathbf{b}_n(\theta_1, \phi) \\ \vdots \\ \mathbf{b}_1(\theta_k, \phi) \\ \vdots \\ \mathbf{b}_n(\theta_k, \phi) \end{bmatrix}_{kn\times 1},$$

$$\mathbf{R}_{Q_{\mathrm{PN}}} = \begin{bmatrix} (\Delta\frac{1}{Q_{\mathrm{PN}}})_1 \\ \vdots \\ (\Delta\frac{1}{Q_{\mathrm{PN}}})_n \end{bmatrix}_{n\times 1}, \ \mathbf{R}_{Q_{\mathrm{SN}}} = \begin{bmatrix} (\Delta\frac{1}{Q_{\mathrm{SN}}})_1 \\ \vdots \\ (\Delta\frac{1}{Q_{\mathrm{SN}}})_n \end{bmatrix}_{n\times 1}, \ \mathbf{R}_{\Delta_{\mathrm{N}}} = \begin{bmatrix} \delta^1_{\Delta_{\mathrm{N}}} \\ \vdots \\ \delta^n_{\Delta_{\mathrm{N}}} \end{bmatrix}_{n\times 1}, \ \mathbf{R}_{\Delta_{\mathrm{T}}} = \begin{bmatrix} \delta^1_{\Delta_{\mathrm{T}}} \\ \vdots \\ \delta^n_{\Delta_{\mathrm{T}}} \end{bmatrix}_{n\times 1},$$

$$\mathbf{A} = \begin{bmatrix} \mathbf{A}_{Q_{\mathrm{PN}}}(\phi_2) - \mathbf{A}_{Q_{\mathrm{PN}}}(\phi_1) & \mathbf{A}_{Q_{\mathrm{SN}}}(\phi_2) - \mathbf{A}_{Q_{\mathrm{SN}}}(\phi_1) & \mathbf{A}_{\Delta_{\mathrm{N}}}(\phi_2) - \mathbf{A}_{\Delta_{\mathrm{N}}}(\phi_1) & \mathbf{A}_{\Delta_{\mathrm{T}}}(\phi_2) - \mathbf{A}_{\Delta_{\mathrm{T}}}(\phi_1) \\ \mathbf{A}_{Q_{\mathrm{PN}}}(\phi_3) - \mathbf{A}_{Q_{\mathrm{PN}}}(\phi_1) & \mathbf{A}_{Q_{\mathrm{SN}}}(\phi_3) - \mathbf{A}_{Q_{\mathrm{SN}}}(\phi_1) & \mathbf{A}_{\Delta_{\mathrm{N}}}(\phi_3) - \mathbf{A}_{\Delta_{\mathrm{N}}}(\phi_1) & \mathbf{A}_{\Delta_{\mathrm{T}}}(\phi_3) - \mathbf{A}_{\Delta_{\mathrm{T}}}(\phi_1) \\ \mathbf{A}_{Q_{\mathrm{PN}}}(\phi_4) - \mathbf{A}_{Q_{\mathrm{PN}}}(\phi_1) & \mathbf{A}_{Q_{\mathrm{SN}}}(\phi_4) - \mathbf{A}_{Q_{\mathrm{SN}}}(\phi_1) & \mathbf{A}_{\Delta_{\mathrm{N}}}(\phi_4) - \mathbf{A}_{\Delta_{\mathrm{N}}}(\phi_1) & \mathbf{A}_{\Delta_{\mathrm{T}}}(\phi_4) - \mathbf{A}_{\Delta_{\mathrm{T}}}(\phi_1) \\ \mathbf{A}_{Q_{\mathrm{PN}}}(\phi_5) - \mathbf{A}_{Q_{\mathrm{PN}}}(\phi_1) & \mathbf{A}_{Q_{\mathrm{SN}}}(\phi_5) - \mathbf{A}_{Q_{\mathrm{SN}}}(\phi_1) & \mathbf{A}_{\Delta_{\mathrm{N}}}(\phi_5) - \mathbf{A}_{\Delta_{\mathrm{N}}}(\phi_1) & \mathbf{A}_{\Delta_{\mathrm{T}}}(\phi_5) - \mathbf{A}_{\Delta_{\mathrm{T}}}(\phi_1) \end{bmatrix}_{4kn\times 4n},$$

$$\mathbf{A}_{Q_{\mathrm{PN}}}(\phi) = \begin{bmatrix} \mathbf{a}_{Q_{\mathrm{PN}}}(\theta_1, \phi) \\ \vdots \\ \mathbf{a}_{Q_{\mathrm{PN}}}(\theta_k, \phi) \end{bmatrix}_{kn\times n}, \ \mathbf{A}_{Q_{\mathrm{SN}}}(\phi) = \begin{bmatrix} \mathbf{a}_{Q_{\mathrm{SN}}}(\theta_1, \phi) \\ \vdots \\ \mathbf{a}_{Q_{\mathrm{SN}}}(\theta_k, \phi) \end{bmatrix}_{kn\times n}, \ \mathbf{A}_{\Delta_{\mathrm{N}}}(\phi) = \begin{bmatrix} \mathbf{a}_{\Delta_{\mathrm{N}}}(\theta_1, \phi) \\ \vdots \\ \mathbf{a}_{\Delta_{\mathrm{N}}}(\theta_k, \phi) \end{bmatrix}_{kn\times n},$$

$$\mathbf{A}_{\Delta_{\mathrm{T}}}(\phi) = \begin{bmatrix} \mathbf{a}_{\Delta_{\mathrm{T}}}(\theta_1, \phi) \\ \vdots \\ \mathbf{a}_{\Delta_{\mathrm{T}}}(\theta_k, \phi) \end{bmatrix}_{kn\times n}, \ \mathbf{a}_{Q_{\mathrm{PN}}}(\theta, \phi) = \begin{bmatrix} P_{Q_{\mathrm{PN}}}(\theta, \phi, g_1) & & \\ & \ddots & \\ & & P_{Q_{\mathrm{PN}}}(\theta, \phi, g_n) \end{bmatrix}_{n\times n},$$

$$\mathbf{a}_{Q_{\mathrm{SN}}}(\theta, \phi) = \begin{bmatrix} P_{Q_{\mathrm{SN}}}(\theta, \phi, g_1) & & \\ & \ddots & \\ & & P_{Q_{\mathrm{SN}}}(\theta, \phi, g_n) \end{bmatrix}_{n\times n},$$

$$\mathbf{a}_{\Delta_{\mathrm{N}}}(\theta,\phi) = \begin{bmatrix} P_{\Delta_{\mathrm{N}}}(\theta,\phi,g_1) & & \\ & \ddots & \\ & & P_{\Delta_{\mathrm{N}}}(\theta,\phi,g_n) \end{bmatrix}_{n\times n},$$

$$\mathbf{a}_{\Delta_{\mathrm{T}}}(\theta,\phi) = \begin{bmatrix} P_{\Delta_{\mathrm{T}}}(\theta,\phi,g_1) & & \\ & \ddots & \\ & & P_{\Delta_{\mathrm{T}}}(\theta,\phi,g_n) \end{bmatrix}_{n\times n}. \tag{26}$$

In order to solve the inverse problem, we employ the Bayesian theorem to make a probabilistic estimation of the unknown parameter vector $\mathbf{X}$ involving the integrated attenuation factors and fracture weaknesses from the input data (i.e. seismic amplitude differences between the data at different azimuthal angles) and a priori information. The posterior probability distribution function (PDF), $P(\mathbf{X}|\mathbf{B})$, of the unknown parameter vector is given by

$$P(\mathbf{X}|\mathbf{B}) \propto P(\mathbf{B}|\mathbf{X})P(\mathbf{X}), \tag{27}$$

where $P(\mathbf{B}|\mathbf{X})$ and $P(\mathbf{X})$ are the likelihood function and prior information PDF.

Assuming uniform uncorrelated Gaussian noise included in observed seismic data, we express the likelihood function as

$$P(\mathbf{B}|\mathbf{X}) = \frac{1}{\sqrt{2\pi\sigma^2_{\mathrm{noise}}}}\exp\left[\frac{-(\mathbf{B}-\mathbf{A}\mathbf{X})^{\mathrm{T}}(\mathbf{B}-\mathbf{A}\mathbf{X})}{2\sigma^2_{\mathrm{noise}}}\right], \tag{28}$$

where $\sigma^2_{\mathrm{noise}}$ is the variance of the noise.

We assume the prior information to follow the Cauchy distribution, which can generate much sparse values that are helpful to produce high-accuracy inversion results (Alemie and Sacchi, 2011; Chen et al., 2017a)

$$P(\mathbf{X}) = \frac{1}{\sqrt{2\pi\sigma^2_{\mathbf{X}}}}\exp\left[-\ln\left(1+\frac{\mathbf{X}^2}{2\sigma^2_{\mathbf{X}}}\right)\right], \tag{29}$$

where $\sigma^2_{\mathbf{X}}$ is the variance of the unknown parameter vector.

Combining equations 5 and 29 yields the posterior PDF

$$P(\mathbf{B}|\mathbf{X}) = \frac{1}{\sqrt{2\pi\sigma^2_{\mathrm{noise}}}}\frac{1}{\sqrt{2\pi\sigma^2_{\mathbf{X}}}}\exp[-J(\mathbf{X})], \tag{30}$$

where

$$J(\mathbf{X}) = \frac{(\mathbf{B}-\mathbf{A}\mathbf{X})^{\mathrm{T}}(\mathbf{B}-\mathbf{A}\mathbf{X})}{2\sigma^2_{\mathrm{noise}}} + \ln\left(1+\frac{\mathbf{X}^2}{2\sigma^2_{\mathbf{X}}}\right), \tag{31}$$

In order to obtain the maximum posterior probability, we should minimize the function $J(\mathbf{X})$. The objective function is given by

$$\frac{\partial J(\mathbf{X})}{\partial \mathbf{X}} = 0. \tag{32}$$

After some algebraic operations, we rewrite equation 32 as

$$\left(\mathbf{A}^{\mathrm{T}}\mathbf{A} + \frac{4\sigma^2_{\mathrm{noise}}}{1 + \dfrac{\mathbf{X}^2}{2\sigma^2_{\mathbf{X}}}} \right) \mathbf{X} = \mathbf{A}^{\mathrm{T}}\mathbf{B}. \tag{33}$$

Equation 33 is nonlinear. In this study, we employ an iterative approach to obtain the inversion result

$$\mathbf{X}_{\mathrm{i}+1} = \mathbf{X}_{\mathrm{i}} + \left(\mathbf{A}^{\mathrm{T}}\mathbf{A} + \frac{4\sigma^2_{\mathrm{noise}}}{1 + \dfrac{{\mathbf{X}_{\mathrm{i}}}^2}{2\sigma^2_{\mathbf{X}_{\mathrm{i}}}}} \right)^{-1} \mathbf{A}^{\mathrm{T}}(\mathbf{B} - \mathbf{A}\mathbf{X}_{\mathrm{i}}), \tag{34}$$

where $\mathbf{X}_{\mathrm{i}+1}$ is the calculated result based on the i^{th} solution $\mathbf{X}_{\mathrm{i}}$, which is reserved as the final inversion result. In addition, $\mathbf{X}_1$ is the initial solution of the unknown parameter vector, which is constructed using the inversion results of P- and S-wave moduli.

RESULTS

Synthetic examples

P- and S-wave moduli and density of a well log model are plotted in Figure 3a. Using the relationship between P-wave inverse quality factor and velocity given by Haase and Stewart (2004), we first compute the P-wave quality factor and then calculate the S-wave quality factor using equation 11. The calculated P- and S-wave quality factors are used as the integrated quality factors of the well log model, as shown in Figure 3b. Given a fracture density curve, we calculate the normal and tangential fracture weaknesses in the case of assuming $\widetilde{\Psi}(\omega)$ and $\widetilde{\Omega}(\omega)$ to be zero, as plotted in Figure 3c.

Given the incidence angle θ range 2°-40°, we first use a 35 Hz wavelet and the elastic parameters (P- and S-wave moduli and density) of the well log model to generate the isotropic and elastic part of synthetic seismic data, and given five azimuthal angles ($\phi_1 = 0^\circ$, $\phi_2 = 30^\circ$, $\phi_3 = 60^\circ$, $\phi_4 = 90^\circ$ and $\phi_5 = 120^\circ$), we use the inverse quality factors and fracture weaknesses of the model to generate the anisotropic and attenuative part of synthetic data. We also add Gaussian random noise with different SNRs (SNRs of 5 and 2) into two parts of the synthetic seismic data respectively. Figure 4a plots the isotropic and elastic part of the synthetic data, and Figure 4b shows differences among synthetic data of different azimuthal angles.

Using the iterative damped least-squares algorithm as outlined in the previous section, we first estimate P- and S-wave moduli from the isotropic and elastic part of synthetic data. Comparisons between the estimated results and true values for the case of SNRs of 5 and 2 are shown in Figures 5a and 5b. In Figure 5c, we plot the relative difference $R(m)$ between the estimated result and the true value (i.e. $\dfrac{m_{\mathrm{estimated}} - m_{\mathrm{true}}}{m_{\mathrm{true}}}$).

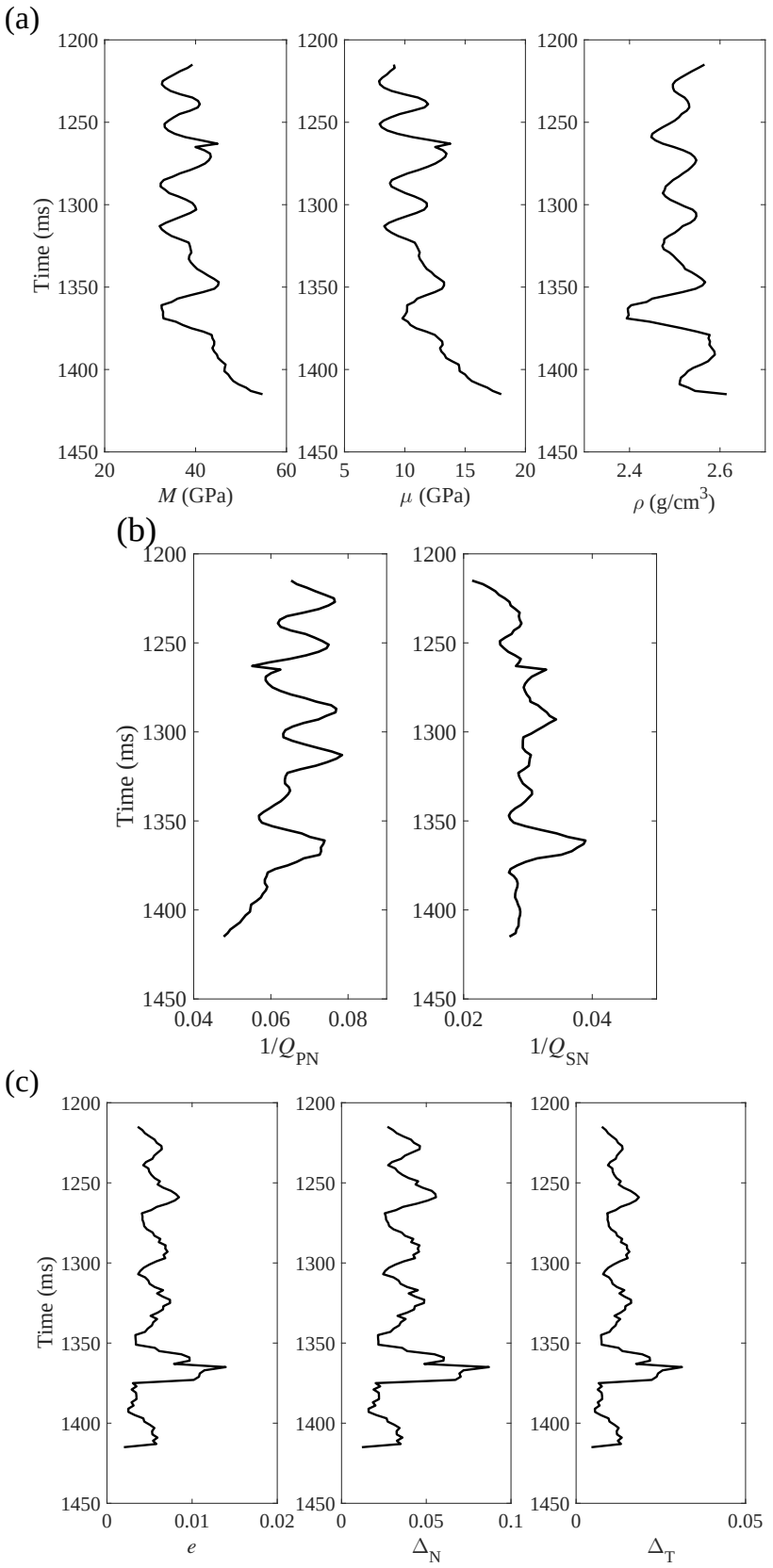

FIG. 3. A well log model involving P- and S-wave moduli (M and μ), density (ρ), calculated inverse quality factors ($1/Q_{\mathrm{P}}$ and $1/Q_{\mathrm{S}}$), given fracture density (e), and computed fracture weaknesses (Δ_{N} and Δ_{T}).

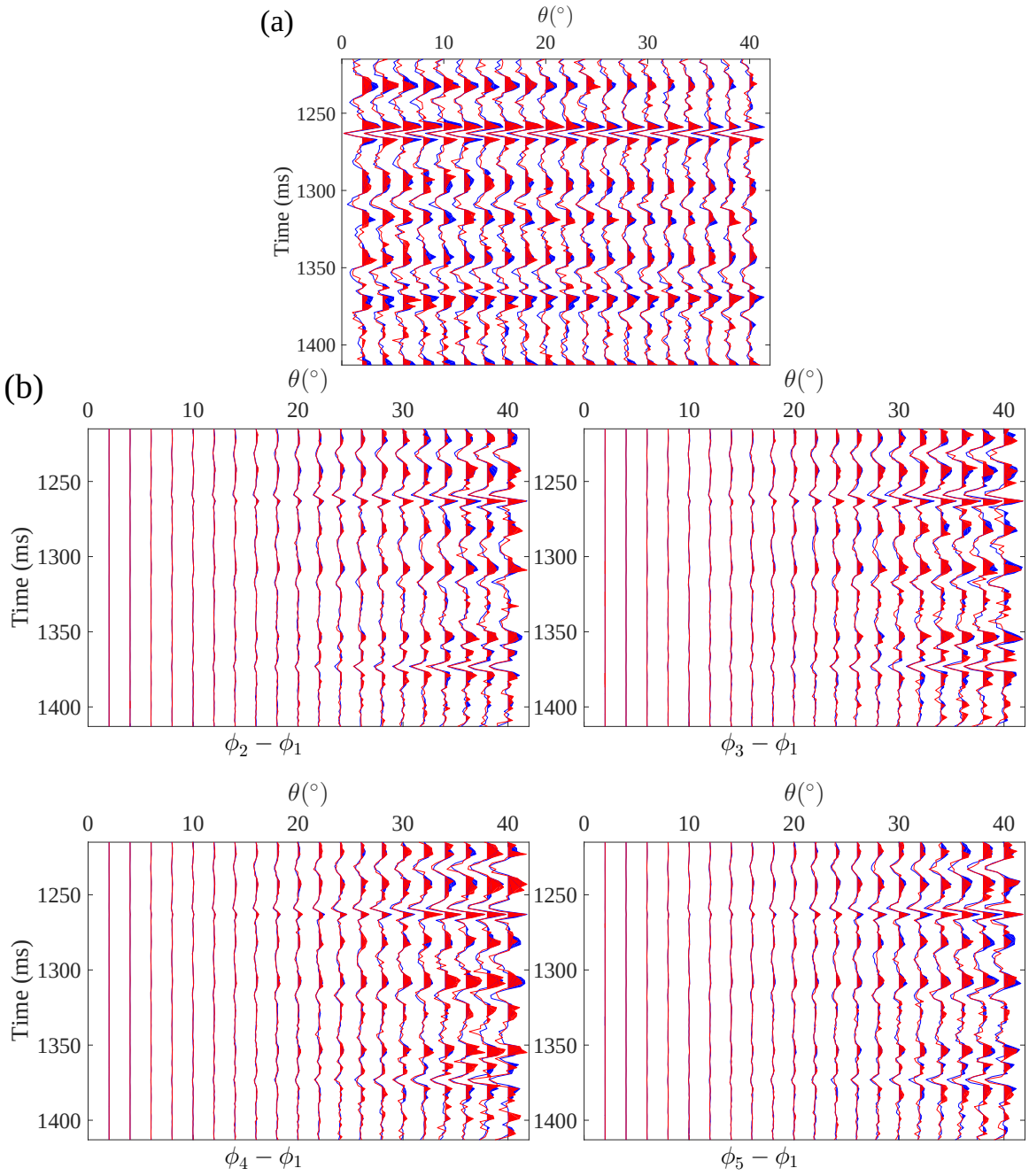

FIG. 4. Synthetic seismic profiles. (a) Isotropic and elastic part of seismic data, and (b) Differences among synthetic data of different azimuthal angles. The blue color represents the SNR of 5, and the red color represents the SNR of 2.

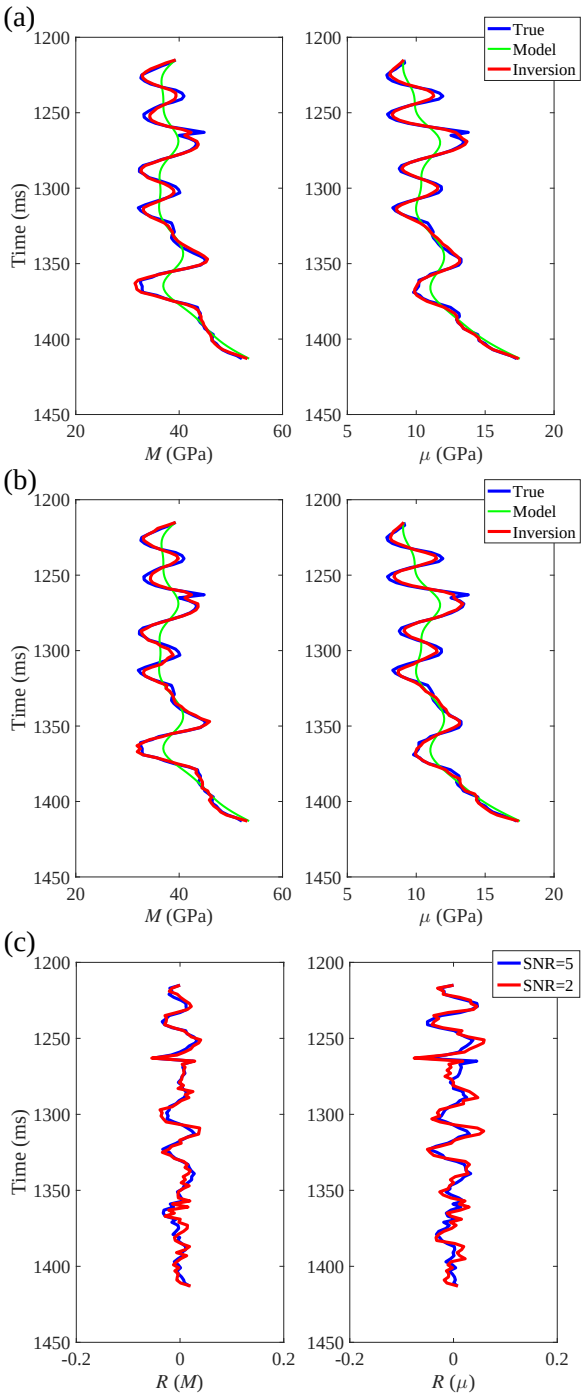

FIG. 5. Comparisons between the estimated results and the true values. Figures (a) and (b) plot the comparisons between the estimated results (red) and true values (blue) for the case of SNRs of 5 and 2, respectively, and green lines represent initial models that are constructed smoothing the true values. Figure (c) shows the comparison between the relative difference for the case of SNR of 5 (blue) and that for the case of SNR of 2 (red).

We observe that the presented iterative damped least-squares algorithm makes a stable estimation of P- and S-wave moduli in the presence of moderate data error/noise (the SNR of 2). From the seismic amplitude differences as shown in Figure 4b, we see that seismic amplitude differences at the small incidence angles are relatively weak. Hence, we choose the seismic amplitude differences at the middle and large incidence angles (80 400) to implement the inversion for the integrated attenuation factors and fracture weaknesses using the proposed approach in the previous section. Figure 6 plots comparisons between the inversion results and true values of the inverse quality factors and fracture weaknesses again for the case of SNRs of 5 and 2.

From the comparison between the inversion result and the true value, we observe that the proposed approach can make a reasonable estimation of integrated attenuation factors and fracture weaknesses. From the difference between the inversion result and the true value, we observe that the accuracy of $1/Q_{\mathrm{PN}}$ inversion is relatively higher than that of $1/Q_{\mathrm{SN}}$ inversion, and the accuracy of Δ_{N} inversion is also relatively higher than that of Δ_{T} inversion.

Inversion of real data

We next utilize a real dataset acquired over a fractured carbonate rock reservoir, which is respectively processed in offset and azimuth domains, to further verify the proposed two-step inversion approach. The azimuthal angles for this dataset are $\phi_1 = 10^\circ$, $\phi_2 = 50^\circ$, $\phi_3 = 90^\circ$, $\phi_4 = 130^\circ$ and $\phi_5 = 170^\circ$, and AVO and AVOA-compliant processing have been implemented for this dataset. In addition, the data set has been transformed from the offset domain to the incidence angle domain for each azimuthal sector. In order to estimate P- and S-wave moduli, we first determine the approximate azimuthal angle of the fracture orientation. Figure 7 plots the main orientation of faults and fractures in this work area.

We observe that the main fracture orientation azimuth is approximately 15°. Hence, we choose the seismic data at the azimuthal angle 10° to estimate P- and S-wave moduli. Figure 8a plots examples of seismic angles gathers at the azimuthal angle 10°, and Figure 8b plots seismic data stacked using the angle gathers. The time-integrated P-wave velocity curve from well logging data has been spliced. We observe that there is a strong reflection in the location of fractured reservoir (around 2080 ms), as marked by the ellipse, and the P-wave velocity shows a relatively low value in the location of the reservoir.

Prior to the first-step inversion, we employ a commercial software package to extract seismic wavelet and roughly predict P- and S-wave moduli and density, and the smoothed version of the roughly estimated results are used as initial models in the iterative damped least-squares inversion. Figure 9 plots the initial models of P- and S-wave moduli for the time window 2050-2150 ms.

Using the extracted wavelet, we implement the iterative damped least-squares inversion for P- and S-wave moduli from seismic angle gathers at the azimuthal angle 10°, as shown in Figure 10.

We observe that P- and S-wave moduli show relatively low values in the location of the

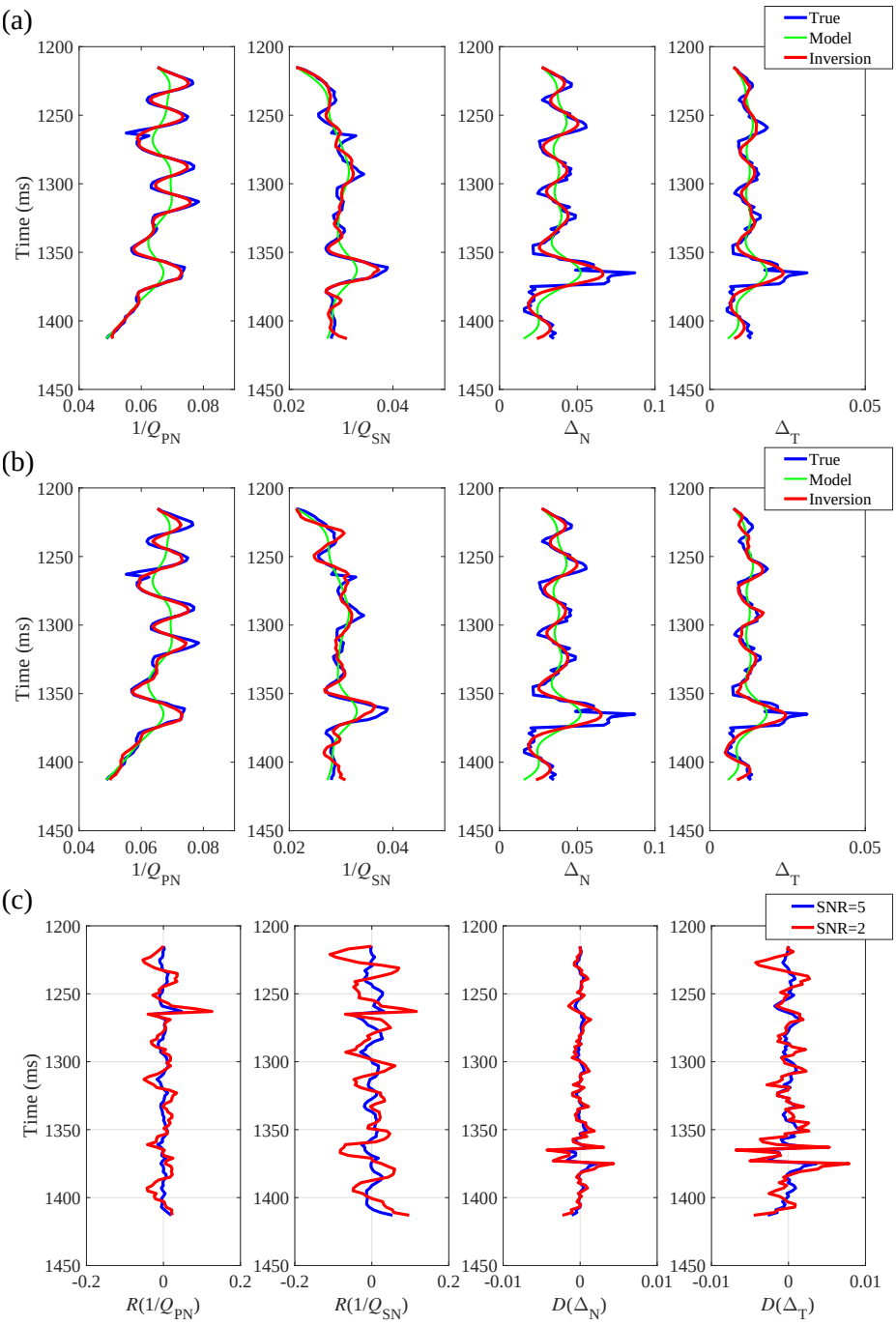

FIG. 6. Comparisons between the inversion results and the true values. Figures (a) and (b) plot the comparisons between the inversion results (red) and true values (blue) of the integrated attenuation factors and fracture weaknesses for the case of SNRs of 5 and 2, respectively, and green lines represent initial models that are constructed smoothing the true values. Figure (c) shows the comparison between the relative differences $R(1/Q_{\mathrm{PN}})$ and $R(1/Q_{\mathrm{SN}})$, the differences $D(\Delta_{\mathrm{N}})$ and $D(\Delta_{\mathrm{T}})$ again for the case of SNRs of 5 and 2. The difference $D(\Delta_{\mathrm{N}})$ is calculated using the equation $\Delta_{\mathrm{N}_{\mathrm{estimated}}} - \Delta_{\mathrm{N}_{\mathrm{true}}}$.

fractured reservoir. We next use seismic amplitude differences to implement the second-step inversion for the integrated attenuation factors and fracture weaknesses. Figure 11 plots examples of angle gather amplitude differences and stacked seismic amplitude differ-

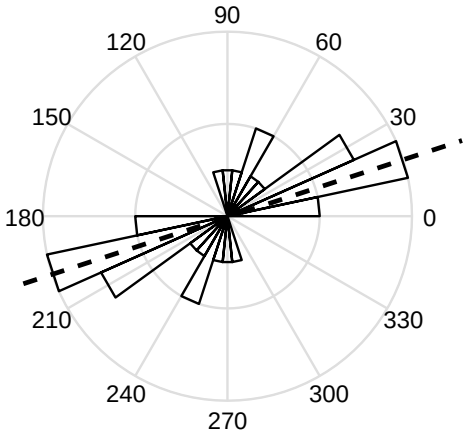

FIG. 7. Main orientation of subsurface faults and fractures in this work area.

ences among the data at different azimuthal angles. We observe that there is still a relatively strong seismic reflection in the location of the fractured reservoir.

We proceed to the construction of initial models for the integrated attenuation factors and fracture weaknesses. Using the inversion results of P- and S-wave moduli, we first employ the experimental equation proposed by Haase and Stewart (2004) to calculate P-wave inverse quality factor roughly, and then calculate S-wave inverse quality factor using equation 11. The smoothed version of the estimated results of P- and S-wave inverse quality factors are using as initial models of the integrated attenuation factors. Given a fracture density, we use the inversion results of P- and S-wave moduli to calculate the normal and tangential fracture weaknesses roughly, and then construct the initial models for fracture weaknesses using the roughly calculated results. Figure 12 plots the constructed initial models of integrated attenuation factors and fracture weaknesses.

Using the Bayesian inversion as presented in the previous section, we implement the iterative inversion for the integrated attenuation factors and fracture weaknesses. Figure 13 plots the inversion results of integrated attenuation factors and fracture weaknesses.

From Figure 13, we observe that there is a good match between P-wave velocity curve and the inversion result. In the location of the fractured reservoir, the integrated attenuation factors and fracture weaknesses show relatively high values. From the inversion results of integrated attenuation factors, we see that the distinction between the fractured reservoir and non-fractured areas is clearer. We conclude that combining the inverted integrated attenuation factors and the inverted fracture weaknesses, we may delineate a fractured reservoir more reliably. However, there are some areas in the inversion results exhibiting high values of fracture weaknesses and integrated attenuation factors, which will require further determination using well-logging and core data.

CONCLUSIONS

We begin with the derivation and simplification of stiffness parameters for fractured and attenuative rocks, and present the integrated attenuation factors involving the intrinsic attenuation of the host rock and fracture-induced attenuation. Using perturbations in stiff-

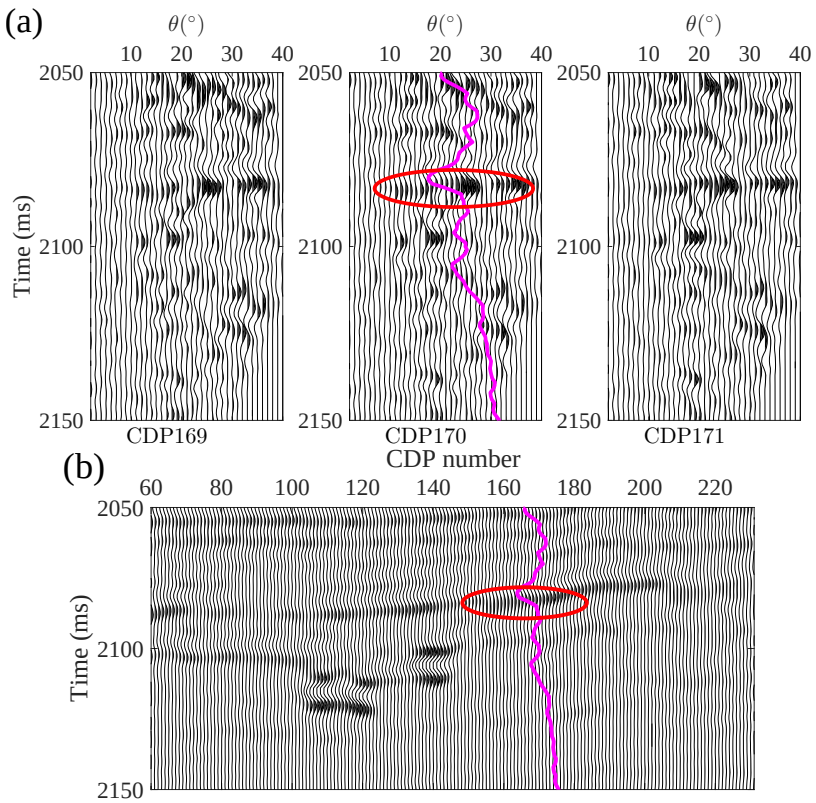

FIG. 8. Angle gathers and stacked seismic profile at the azimuthal angle $10°$. (a) Examples of seismic angle gathers, and (b) Seismic profile stacked using the angle gathers. The curve represents the time-integrated P-wave velocity.

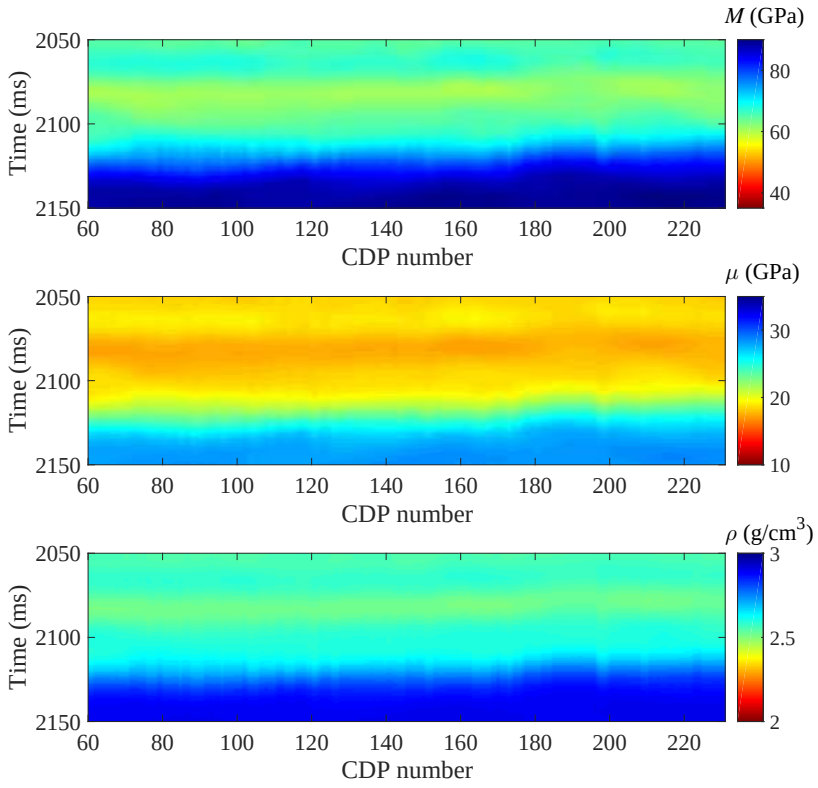

FIG. 9. Initial models of P- and S-wave moduli and density.

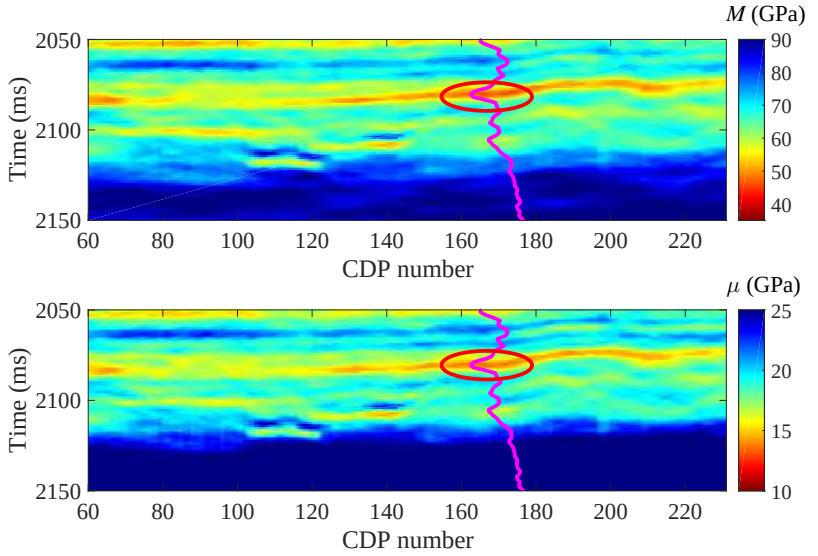

FIG. 10. Inversion results of P- and S-wave moduli. The ellipse represents the location of the fractured reservoir.

ness parameters for the case of an interface separating two fractured and attenuative media, we derive a linearized reflection coefficient in terms of P- and S-wave moduli, integrated attenuation factors and fracture weaknesses. Based on the derived reflection coefficient, we propose a two-step inversion method to use azimuthal seismic data to estimate fracture weaknesses and integrated attenuation factors, which is implemented as: 1) utilizing seismic data at the azimuthal angle equal or approximately equal to fracture orientation

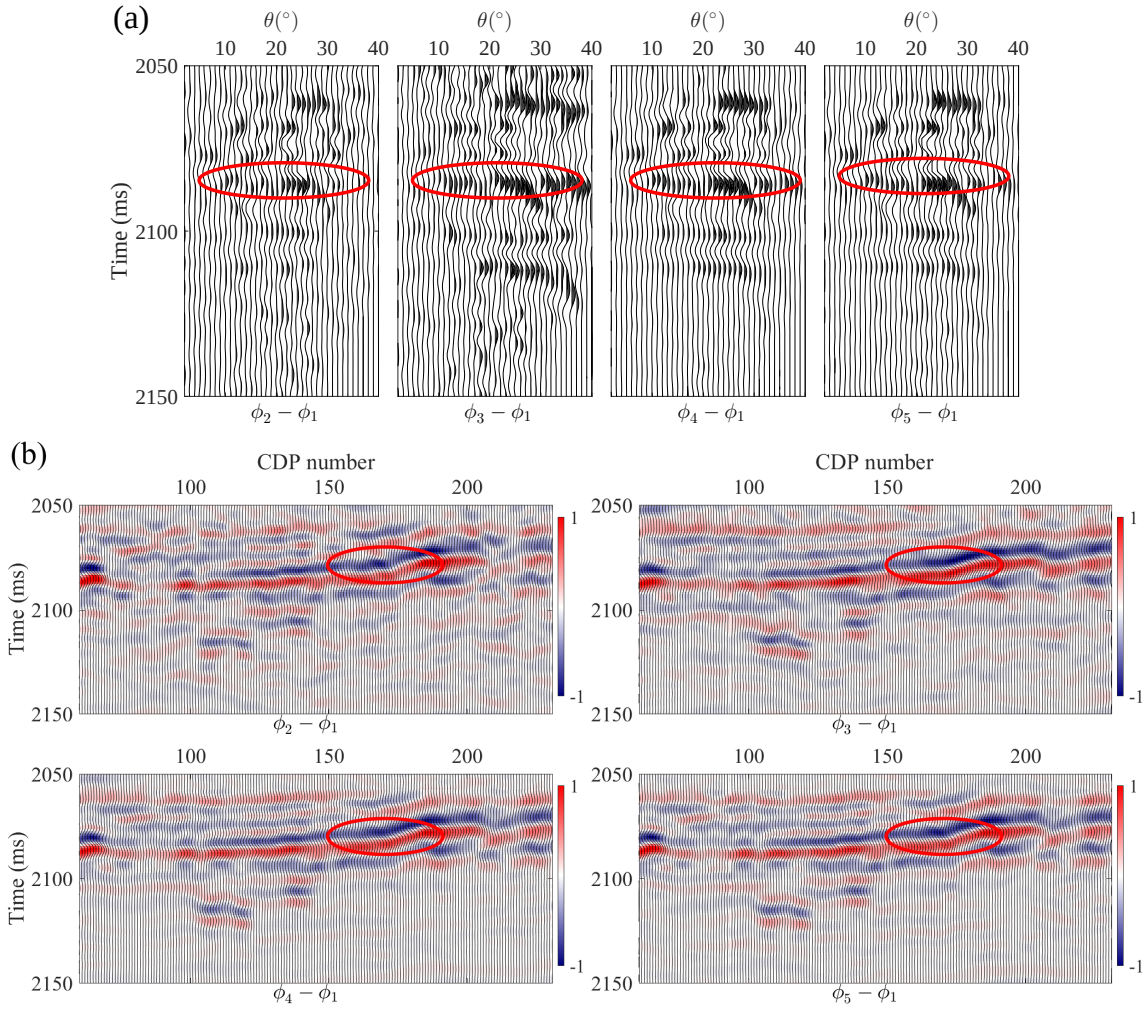

FIG. 11. Seismic amplitude differences among the data at different azimuthal angles. (a) Angle gather amplitude differences at CDP 140, and (b) Stacked seismic amplitude differences. The ellipse indicates the location of the fractured reservoir.

azimuth to predict elastic parameters (P- and S-wave moduli) using an iterative damped ; 2) employing seismic amplitude differences among the data at different azimuthal angles to estimate the integrated attenuation factors and fracture weaknesses using an iterative Bayesian inversion. Applying the proposed inversion method to synthetic seismic data, we conclude that P- and S-wave moduli, integrated attenuation factors and fracture weaknesses can be estimated stably in the case of moderate noise/error ($\mathrm{SNR} \geq 2$). A test on a real data set acquired over a fractured carbonate reservoir reveals that the proposed inversion method can provide realistic results of integrated attenuation factors and fracture weaknesses for fracture prediction and fluid discrimination.

There are some assumptions under which we derive the linearized reflection coefficient and apply the two-step inversion approach. Firstly, the normal and tangential fracture weaknesses are small, and their changes across the interface are small; secondly, the host rock is assumed to be a low-loss medium; thirdly, we neglect the imaginary part of the reflection coefficient which is smaller than the real part. These assumptions restrict the applicability

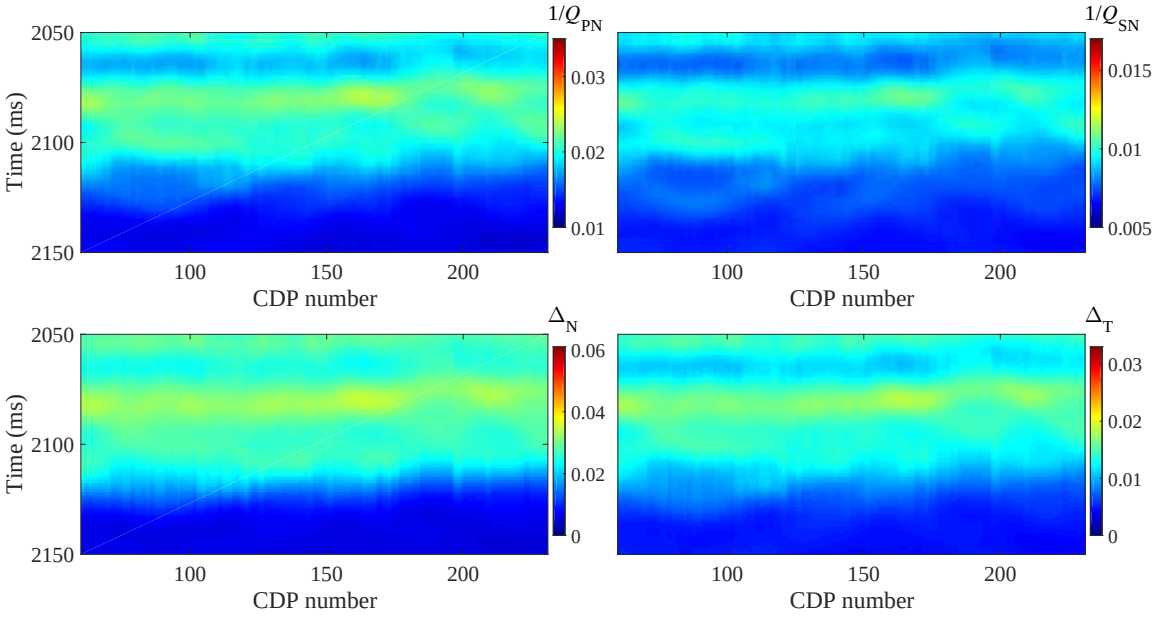

FIG. 12. Initial models of integrated attenuation factors and fracture weaknesses.

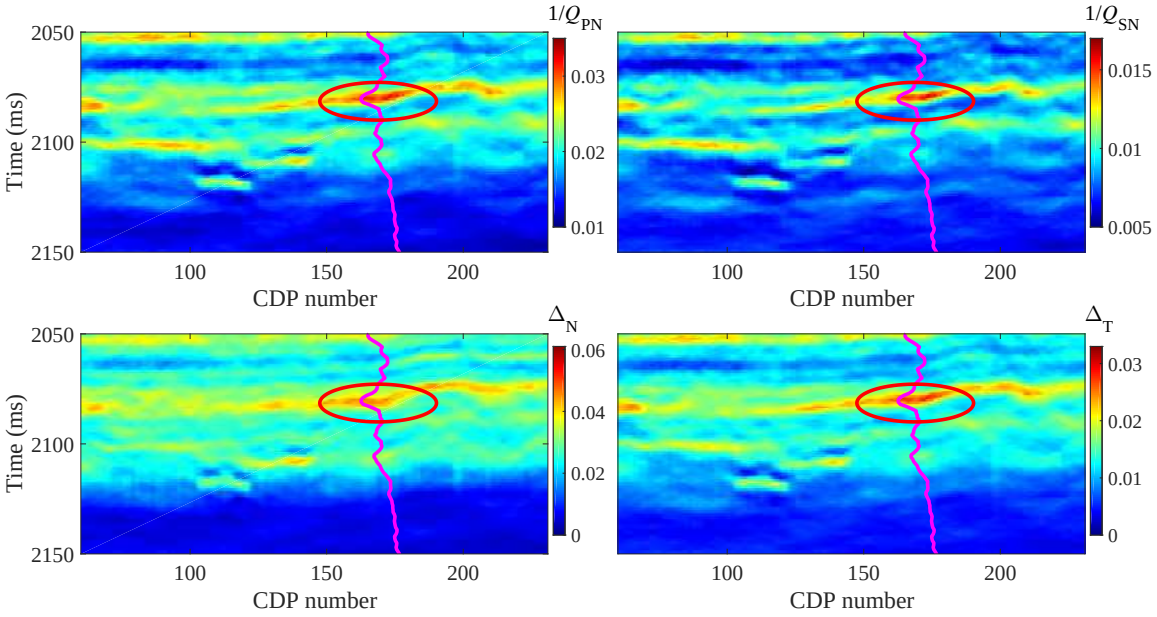

FIG. 13. Inversion results of integrated attenuation factors and fracture weaknesses. The curve is P-wave velocity

of the reflection coefficient and the proposed inversion method, however, the fractured oil-bearing carbonate reservoir falls into this category. Although quantitative parameters for fluid or fractures don't emerge from our approach, inversion results of integrated attenuation factors can be preserved as reasonable information for determine fluid type based on rock physics.

APPENDIX A. EXPRESSIONS OF $\widetilde{\Psi}$ AND $\widetilde{\Omega}$ RELATED TO FRACTURE ASPECT RATIO AND FLUID BULK MODULUS

Pointer et al. (2000) presented expressions of $\widetilde{\Psi}(\omega)$ and $\widetilde{\Omega}(\omega)$ in the case of an equant porosity model

$$\begin{aligned}\widetilde{\Psi}(\omega) &= \frac{1}{\pi}\frac{a}{c}\frac{K_f}{\mu}\frac{1}{1-g}/[1+3(1-i)\frac{\vartheta}{2c}],\\ \widetilde{\Omega}(\omega) &= \frac{4}{\pi}\frac{i\omega\eta_f}{\mu}\frac{1}{3-2g},\end{aligned} \tag{A.1}$$

where a/c is fracture aspect ratio, K_f is bulk modulus of the filling fluid, and η_f is fluid viscosity.

ACKNOWLEDGEMENTS

The industrial sponsors of CREWES are thanked for their support. We gratefully acknowledge support from NSERC (Natural Science and Engineering Research Council of Canada) through the grant CRDPJ 461179-13. This research was undertaken thanks in part to funding from the Canada First Research Excellence Fund and Mitacs Project. The SINOPEC Key Lab of Multi-Component Seismic Technology is thanked for providing the data. Hampson-Russell software was used to construct the initial model and carry out the wavelet extraction.

REFERENCES

Alemie, W., and Sacchi, M. D., 2011, High-resolution three-term avo inversion by means of a trivariate cauchy probability distribution: Geophysics, **76**, No. 3, R43–R55.

Bachrach, R., Sengupta, M., Salama, A., and Miller, P., 2009, Reconstruction of the layer anisotropic elastic parameters and high-resolution fracture characterization from p-wave data: a case study using seismic inversion and bayesian rock physics parameter estimation: Geophysical prospecting, **57**, No. 2, 253–262.

Bakulin, A., Grechka, V., and Tsvankin, I., 2000, Estimation of fracture parameters from reflection seismic data–part i: Hti model due to a single fracture set: Geophysics, **65**, No. 6, 1788–1802.

Brajanovski, M., Müller, T. M., and Gurevich, B., 2006, Characteristic frequencies of seismic attenuation due to wave-induced fluid flow in fractured porous media: Geophysical Journal International, **166**, No. 2, 574–578.

Chapman, M., 2003, Frequency-dependent anisotropy due to meso-scale fractures in the presence of equant porosity: Geophysical Prospecting, **51**, No. 5, 369–379.

Chen, H., and Innanen, K. A., 2017, Seismic inversion for p-and s-wave inverse quality factors using attenuative elastic impedance, *in* SEG Technical Program Expanded Abstracts 2017, Society of Exploration Geophysicists, 646–650.

Chen, H., Ji, Y., and Innanen, K. A., 2017a, Estimation of modified fluid factor and dry fracture weaknesses using azimuthal elastic impedance: Geophysics, **83**, No. 1, 1–74.

Chen, H., Yin, X., Qu, S., and Zhang, G., 2014a, Avaz inversion for fracture weakness parameters based on the rock physics model: Journal of Geophysics and Engineering, **11**, No. 6, 065,007.

Chen, H., Zhang, G., Chen, J., and Yin, X., 2014b, Fracture filling fluids identification using azimuthally elastic impedance based on rock physics: Journal of Applied Geophysics, **110**, 98–105.

Chen, H., Zhang, G., Ji, Y., and Yin, X., 2017b, Azimuthal seismic amplitude difference inversion for fracture weakness: Pure and Applied Geophysics, **174**, No. 1, 279–291.

Chichinina, T., Obolentseva, I., Gik, L., Bobrov, B., and Ronquillo-Jarillo, G., 2009, Attenuation anisotropy in the linear-slip model: Interpretation of physical modeling data: Geophysics, **74**, No. 5, WB165–WB176.

Chichinina, T., Sabinin, V., and Ronquillo-Jarillo, G., 2006, Qvoa analysis: P-wave attenuation anisotropy for fracture characterization: Geophysics, **71**, No. 3, C37–C48.

Downton, J., and Roure, B., 2010, Azimuthai simultaneous elastic inversion for fracture detection, *in* SEG Technical Program Expanded Abstracts 2010, Society of Exploration Geophysicists, 263–267.

Downton, J. E., and Roure, B., 2015, Interpreting azimuthal fourier coefficients for anisotropic and fracture parameters: Interpretation, **3**, No. 3, ST9–ST27.

Dvorkin, J., Mavko, G., and Nur, A., 1995, Squirt flow in fully saturated rocks: Geophysics, **60**, No. 1, 97–107.

Gautam, K., 2003, Fluid effects on attenuation and dispersion of elastic waves: Ph.D. thesis, Colorado School of Mines.

Gurevich, B., 2003, Elastic properties of saturated porous rocks with aligned fractures: Journal of Applied Geophysics, **54**, No. 3, 203–218.

Haase, A. B., and Stewart, R. R., 2004, Attenuation estimates from vsp and log data, *in* SEG Technical Program Expanded Abstracts 2004, Society of Exploration Geophysicists, 2497–2500.

Hudson, J., 1980, Overall properties of a cracked solid: Mathematical Proceedings of the Cambridge Philosophical Society, **88**, No. 2, 371–384.

Hudson, J., Liu, E., and Crampin, S., 1996, The mechanical properties of materials with interconnected cracks and pores: Geophysical Journal International, **124**, No. 1, 105–112.

Klimentos, T., and McCann, C., 1990, Relationships among compressional wave attenuation, porosity, clay content, and permeability in sandstones: Geophysics, **55**, No. 8, 998–1014.

Mavko, G., Mukerji, T., and Dvorkin, J., 2009, The rock physics handbook: Tools for seismic analysis of porous media: Cambridge university press.

Moradi, S., and Innanen, K. A., 2015, Scattering of homogeneous and inhomogeneous seismic waves in low-loss viscoelastic media: Geophysical Journal International, **202**, No. 3, 1722–1732.

Pan, X., Zhang, G., and Yin, X., 2017, Azimuthally anisotropic elastic impedance inversion for fluid indicator driven by rock physics: Geophysics, **82**, No. 6, 1–67.

Pointer, T., Liu, E., and Hudson, J. A., 2000, Seismic wave propagation in cracked porous media: Geophysical Journal International, **142**, No. 1, 199–231.

Rubino, J., and Holliger, K., 2013, Research note: Seismic attenuation due to wave-induced fluid flow at microscopic and mesoscopic scales: Geophysical Prospecting, **61**, No. 4, 882–889.

Rüger, A., 1997, P-wave reflection coefficients for transversely isotropic models with vertical and horizontal axis of symmetry: Geophysics, **62**, No. 3, 713–722.

Rüger, A., 1998, Variation of p-wave reflectivity with offset and azimuth in anisotropic media: Geophysics, **63**, No. 3, 935–947.

Schoenberg, M., and Douma, J., 1988, Elastic wave propagation in media with parallel fractures and aligned cracks: Geophysical Prospecting, **36**, No. 6, 571–590.

Schoenberg, M., and Sayers, C. M., 1995, Seismic anisotropy of fractured rock: Geophysics, **60**, No. 1, 204–211.

Shaw, R. K., and Sen, M. K., 2004, Born integral, stationary phase and linearized reflection coefficients in weak anisotropic media: Geophysical Journal International, **158**, No. 1, 225–238.

Shaw, R. K., and Sen, M. K., 2006, Use of avoa data to estimate fluid indicator in a vertically fractured medium: Geophysics, **71**, No. 3, C15–C24.

Thomsen, L., 1986, Weak elastic anisotropy: Geophysics, **51**, No. 10, 1954–1966.

Vinci, C., Renner, J., and Steeb, H., 2014, On attenuation of seismic waves associated with flow in fractures: Geophysical Research Letters, **41**, No. 21, 7515–7523.

Wu, R., and Aki, K., 1989, Scattering and attenuation of seismic waves: Birkhäuser, Basel.